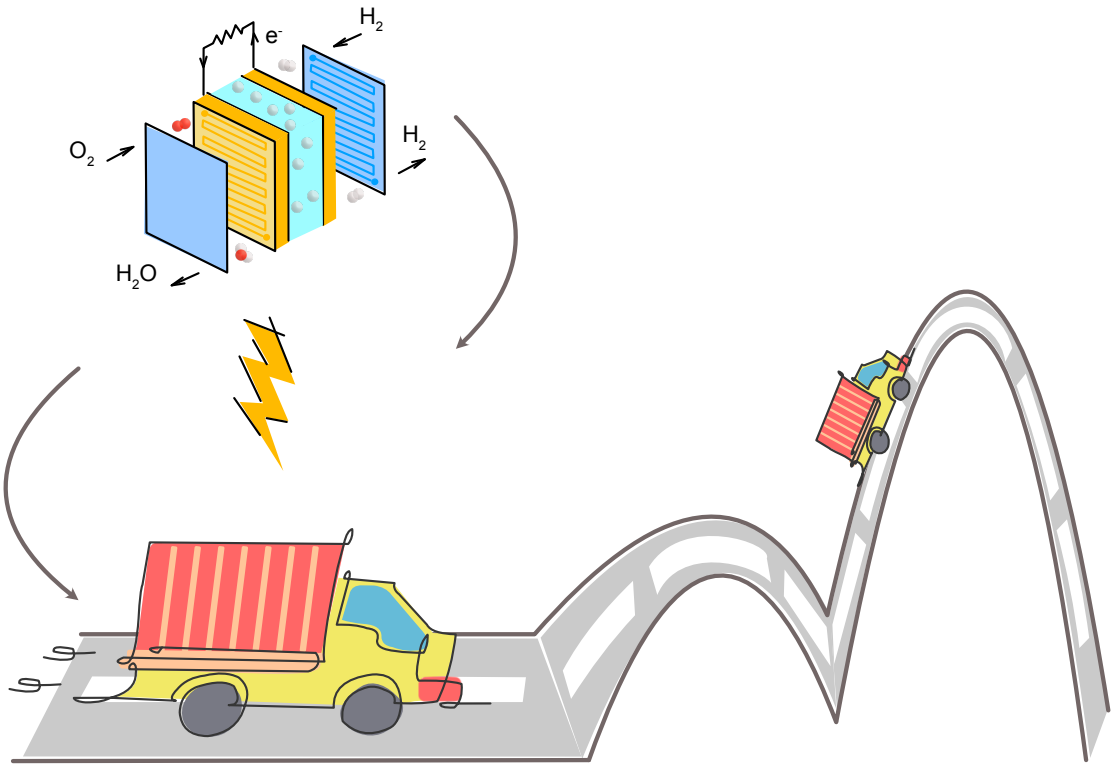

Mission management for fuel cell heavy-duty trucks

Master's thesis in Systems, Control and Mechatronics

DANIEL SUNDBERG

ANDREAS BRAGDE

DEPARTMENT OF ELECTRICAL ENGINEERING

CHALMERS UNIVERSITY OF TECHNOLOGY
Gothenburg, Sweden 2023
www.chalmers.se

Master's thesis 2023

Mission management for fuel cell heavy-duty trucks

ANDREAS BRAGDE
DANIEL SUNDBERG

CHALMERS
UNIVERSITY OF TECHNOLOGY

Department of Electrical Engineering
Division of Systems and control
Chalmers University of Technology
Gothenburg, Sweden 2023

Mission Management for fuel cell heavy-duty trucks
ANDREAS BRAGDE, DANIEL SUNDBERG

Supervisor: Saurabh Suman, Volvo trucks
Examiner: Nikolce Murgovski, Department of Electrical Engineering

Master's Thesis 2023
Department of Electrical Engineering
Chalmers University of Technology
SE-412 96 Gothenburg
Telephone +46 31 772 1000

Cover: Fuel cell truck driving a long-haul mission.

Typeset in LaTeX
Printed by Chalmers Reproservice
Gothenburg, Sweden 2023

Mission Management for fuel cell heavy-duty trucks
ANDREAS BRAGDE, DANIEL SUNDBERG
Department of Electrical Engineering
Chalmers University of Technology

Abstract

Fuel cell electric vehicles (FCEVs) need better fuel economy, increased fuel cell longevity and drivability to be competitive alternatives to traditional internal combustion engine vehicles. This thesis investigates the benefits of an optimal mission planner for heavy-duty fuel cell trucks during long-haul driving missions. Nonlinear model predictive control (NMPC) is used to preoptimise vehicle speed, fuel cell power, battery power, battery state of charge (SOC) and refuelling decisions for a given driving mission. The mission planner is evaluated on a 650 and 520 kilometre driving-cycle. The latter route includes refuelling stations. On these routes, a receding horizon controller is compared to an equivalent controller which utilises the mission planner. It is found that energy consumption is decreased by 13% on the 650 kilometre route and 17% on the 520 kilometre route. It is also found that the mission planner increases drivability and reduces friction break usage in hilly areas.

Keywords: Fuel cell electric vehicles, Nonlinear model predictive control, Optimisation, Eco-driving

Acknowledgements

The authors' want to thank the project supervisor Saurabh Suman for his incessant engagement in this work and the things he taught us. We also want to thank the thesis examiner Nikolce Murgovski for gladly sharing his expertise in numerical optimal control. Many more optimisations would have diverged without him. We also want to thank all of the people who supported us at Volvo AB, especially Staffan Luong, Eva Skvor and Olof Lindegärde who went the extra mile for this project. Finally, we want to thank Noemi Bosio for the illustrations she provided and the academic advice she gave.

Daniel Sundberg, Gothenburg, June 2023
Andreas Bragde, Gothenburg, June 2023

List of Acronyms

Below is the list of acronyms that have been used throughout this thesis listed in alphabetical order:

BEV	Battery electric vehicle
EM	Electric machine
ESS	Energy storage system
HRS	Hydrogen refuelling station
MPC	Model predictive control
NMPC	Nonlinear model predictive control
FC	Fuel cell
FCEV	Fuel cell electric vehicle
PEM	Predictive energy management
PEMFC	Proton-exchange membrane fuel cell
RPM	Revolutions per minute
SoC	Battery state of charge

Nomenclature

Below is the nomenclature of indices, sets, parameters, and variables that have been used throughout this thesis.

Indices

N	Total number of stages in the MPC problem
k	Stage number in the MPC problem
s_0	first station index
s_N	last station index
s_i	general station index

Sets

$\mathcal{X}_0$	Initial state constraint in the MPC problem
$\mathcal{X}$	State constraint in the MPC problem
$\mathcal{X}_N$	Final state constraint in the MPC problem
$\mathcal{U}$	Control input constraint in the MPC problem

Parameters

m	Vehicle mass
$A_{v,f}$	Vehicle effective frontal surface area
C_d	Vehicle aerodynamic drag coefficient
C_{rr}	Vehicle rolling resistance coefficient
r_{eff}	Effective wheel radius of loaded tyre
r_{tm}	Gear ratio of the transmission
g	Gravity

ρ_{air}	Air density
η_{EM}	Electric machine efficiency
η_{tm}	Transmission efficiency
η_{FCDC}	DC-DC converter efficiency, fuel cell to DC bus
$\eta_{B,reg}$	Regenerative breaking efficiency
$P_{FC,max}$	Fuel cell maximum power output
$P_{FC,min}$	Fuel cell minimum idling power output
$\dot{P}_{FC,max}$	Fuel cell maximum power output rate
$\dot{P}_{FC,min}$	Fuel cell minimum power output rate
C_B	Battery capacity
R_B	Battery internal resistance
$P_{B,max}$	Battery maximum power output
$P_{B,min}$	Battery minimum power output
P_{aux}	Auxiliary power demand
N	Number of stages in the MPC problem
s	station
s_f	station fuelling speed
q_t	station queue time

Variables

x	State vector
u	Control input vector
t	Time
v	Vehicle longitudinal velocity
s_p	Vehicle position along the path
SoC	Battery state of charge
H_2	Available hydrogen gas
H_{con}	Amount of hydrogen gas consumed
P_{FC}	Fuel cell power output
P_B	Battery power output
P_C	Cooling power demand
Q_{FC}	Heat generated in fuel cell
Q_B	Heat generated in battery

F_{break}	Service break
δ	arbitrary slack variables
F_T	Traction force
F_{rr}	Rolling resistance force
F_{sx}	Longitudinal slip loss
F_{aero}	Aerodynamic drag force
F_{slope}	Resistive force due to road slope

Functions

$\alpha(s_p)$	road gradient
$v_{lim}(s_p)$	road speed limit
$J(\cdot)$	Objective function to minimise
$f(\cdot)$	State dynamics
$g(\cdot)$	Nonlinear inequality constraints
$r_{EM}(\gamma)$	Gear ratio of motor as a function of gear γ
$S_g(v(t))$	sigmoid activation function

Contents

List of Figures

List of Tables

1
Introduction

1.1 Fuel cell electric vehicles

The Paris Agreement, adopted by 196 Parties at the UN Climate Change conference, entered into force year 2016. Its overarching goal is to limit the average global temperature increase to 1.5 C° above pre-industrial temperatures by the end of the century [1]. For this to be possible, it was stated that greenhouse gas emission must peak before 2025 and decline by 43% year 2030. To achieve this goal, all European countries signed the European Green Deal year 2020. The European Green Deal is a set of policies which aim to make Europe the first climate-neutral continent in the world by year 2050 [2]. Targets included in the deal are a 55% greenhouse gas emission reduction from cars by the year 2030, and zero emissions from new cars by year 2035. The legislation compel automotive manufacturers to research and develop zero-emission vehicles. The long-distance transport sector are required to look beyond battery electric vehicles (BEVs) as their high weight and long charging time make them unsuited for long-haul driving mission. Hydrogen-based fuel cell electric vehicles (FCEVs) are promising alternatives as their driving range and refuelling times are similar to internal combustion engine vehicles (ICEV). They are also classed as zero-emission vehicles as the fuel cell chemical reaction only emits water vapour [3]. A life-cycle assessment, however, provides a more holistic view on the sustainability of FCEVs. In a thorough literature review, the authors of [4] show that FCEVs are more polluting during the manufacturing stage than ICEVs, but between 40% and 80% less during their entire life time.

The drivability and efficiency of FCEVs is improved by adding a short-term energy storage system (ESS) [3]. A lithium-based battery is used in this thesis. The ESS enables regenerative breaking and covers power peaks during acceleration and hill-climbing. The fuel cell is operated almost statically as power fluctuations degrade it and its efficiency depends strongly on output power [5]. To fully utilise the ESS, however, battery state of charge (SoC) must be optimised. Essentially, the battery SoC should be nearly full before demanding uphill climbs, and nearly empty before long downhills. The regenerative breaks cannot be used when the battery SoC is full, in which case friction breaks are applied instead. High friction break usage results in energy loss and poor fuel economy [6].

1.2 Mission management

Mission management may broadly be described as a set of functions which support vehicle operation. The aid may be strategic, such as travel route and departure-time selection or operational, such as powertrain usage. This thesis mainly deals with the latter, i.e. to develop a mission planner that supports on-board control system decision making. An optimal fuelling plan is produced as well, which is best described as strategic. The purpose of the planner is to improve fuel economy, lower trip cost and increase vehicle drivability while ensuring some arrival time. It should be noted that traditional on-board energy management systems base their control on momentaneous sensor reading and possibly past readings. This thesis is developed in an environment where the energy management system has access to *some* look-ahead information. The purpose of the mission management layer is thus to provide important information that the on-board control systems do not have access to.

As mentioned in the previous section, battery SoC optimisation can improve fuel economy by enabling high-efficiency operation of the fuel cell and increased energy recuperation. Vehicle drivability is also increased by SoC optimisation as the available power is increased. The optimal battery SoC depends on the current state of the vehicle and the future road topography. For this reason, the entire driving mission is preoptimised with position-dependent suggestions. It should be noted that SoC optimisation is only one of many ways that mission management can improve fuel economy. Another example is the vehicle speed, which is a large contributing factor as aerodynamic drag is proportional to the square of speed.

Eco-driving and optimal recharging for BEVs and hybrid electric vehicles are well-studied subjects, often utilising nonlinear model predictive control (NMPC). Some examples are [7][8][9][10], which suggest significant energy savings by using energy-optimal predictive control methods. Regarding FCEVs, in a study similar to this thesis, the authors of [11] display energy savings and increase of fuel cell life-time by using a hierarchical MPC structure. The authors of [12] and [13] show that variants of MPC yields significant hydrogen savings and fuel cell life-time improvement over rule base control methods and slightly better performance than dynamic programming. To the authors' knowledge, there is no study on mission-long speed optimisation, predictive power split and SoC-reference generation which includes refuelling decisions for FCEVs. This thesis presents a novel approach to mission management which solves the problem jointly, while keeping complexity down by suitable abstraction and convexification. The solution to refuelling when sampling in space is not found in the literature and is suitable for very large optimisation problems.

1.3 Delimitations

Since most of the concerns when it comes to the viability of heavy duty FCEVs stem from issues that arise in driving cycles which consist mostly of hilly terrain, these cycles will be the focus of this thesis. Truck drivers are legally required by EU regulation to take breaks of 45 minutes every 4 hours [14]. The scheduling of truck drivers is a complex problem of its own and has been studied before [15]. Thus, the scheduling and simulation of these stops are considered outside the thesis scope.

To reduce the size of the problem, only longitudinal dynamics are considered. That is, the road is considered to be straight and forces only act along the axis where the truck is driving and its normal. The driving mission only considers one truck, and no other vehicles along the route.

1.4 Research questions

Based on the description of mission management, the following research questions have been formulated. The main focus of this thesis is in regards to the first question due to the broadness of the formulation.

- What are the limitations and benefits of adding an optimisation layer with full mission information?
- How does a FCEV utilising the mission planner compare, in terms of energy consumption, travel time and trip cost, to an FCEV that does not?
- What is a suitable level of model complexity for FCEV mission management?

2
Vehicle modelling

The vehicle considered in this thesis is a long haul heavy-duty truck with a hybrid powertrain. The main energy source is a fuel cell system, and the secondary a lithium-ion battery. The battery pack is sized to support high output power or regenerative breaking for sufficient time periods. The battery is charged by the fuel cell and cannot be charged via plug-in. This chapter aims to provide the reader with requisite knowledge to follow the remainder of the thesis.

2.1 Longitudinal dynamics

The equation of motion in the travelling direction of the vehicle is

$$m\dot{v} = F_T - F_{rr} - F_{aero} - F_{slope} - F_{break} \tag{2.1}$$

where m is the vehicle mass and $\dot{v}$ is the time-derivative of vehicle speed. On the right-hand side, F_T is the tractive effort generated by the EM, F_{rr} is the rolling resistance force of all wheels, F_{aero} is the aerodynamic drag force and F_{slope} is the force due to road slope. The equation of motion is missing longitudinal slip losses, which arise when the wheel rotation speed differs from the corresponding vehicle speed. The reason for slip loss disclusion is that they are mostly relevant during acceleration and deceleration and require wheel rotation speed states. The increased model complexity is therefore hard to motivate in a mission-management context. Traction effort F_T is further elaborated on in section 2.2 while the other forces are discussed here.

Rolling resistance

Rolling resistance is a result of tyre deformation. As a wheel rotates, new tyre material enters the contact patch and is deflected vertically, resulting in a flat section in contact with the road. When this tyre section rotates further and loses contact with the road, the material springs back into place. The deformation energy is not completely recovered due to internal damping in the tyre material [16]. The amount of deformation, and consequently, energy lost is proportional to the normal force on the tyre. This loss is given by

$$F_{rr} = C_{rr}F_z \tag{2.2}$$

where C_{rr} is the rolling resistance coefficient of each tyre and F_z is the normal force acting on each tyre. The rolling resistance coefficient C_{rr} is a measure of the force needed to push a vehicle at constant speed with zero road grade and zero air

resistance per unit weight. The rolling resistance coefficient is typically determined experimentally and is about 0.0065 for semi-trailers weighing 40 ton [17]. In steady-state conditions, the vertical force is $F_z = mg\cos(\alpha)$, where α is the road grade. The rolling resistance force used in the model is thus

$$F_{rr} = C_{rr} mg \cos(\alpha) \tag{2.3}$$

Aerodynamic drag

Drag forces arise when an object is moving through a fluid. The exerted force is proportional to the square of the difference between the object and fluid speed. The equation is attributed to Lord Rayleigh and is known as quadratic drag.

$$F_{aero} = \frac{1}{2}\rho_{air} C_d A_{v,f} v^2 \tag{2.4}$$

The first parameter ρ_{air} is the density of air, C_d is the aerodynamic drag coefficient and $A_{v,f}$ is the vehicle effective frontal area. The effects of wind speed and wind heading is not part of this thesis' analysis so v is simply the vehicle's longitudinal speed.

Road slope

The force due to road slope is simply the normal component directed in the vehicle heading. It is described by

$$F_{slope} = mg\sin(\alpha) \tag{2.5}$$

Breaking force

The breaking force F_{break} is realised by friction (disc) breaks. The temperature, and consequently, breaking limits are not modelled in this thesis. It should be noted, however, that the breaks *can* overheat and friction break use is, contrary to regenerative breaking, energy lost, so friction break usage should be kept to a minimum.

2.2 Powertrain

2.2.1 Electric motor

The efficiency map of the EM is seen in Figure 2.1. The tractive effort at the wheels F_T, first mentioned in Equation (2.1), is

$$F_T = \frac{\eta_{EM} r_{EM}(\gamma) r_{tm} \tau_{EM}}{r_{eff}} \tag{2.6}$$

where the efficiency η_{EM} depends on the torque and rotation speed of the motor, as seen in Figure 2.1, r_{EM} is the gear ratio of the EM, which depends on the gear γ, r_{tm} is the fixed gear ratio of the transmission and r_{eff} is the effective tyre radius.

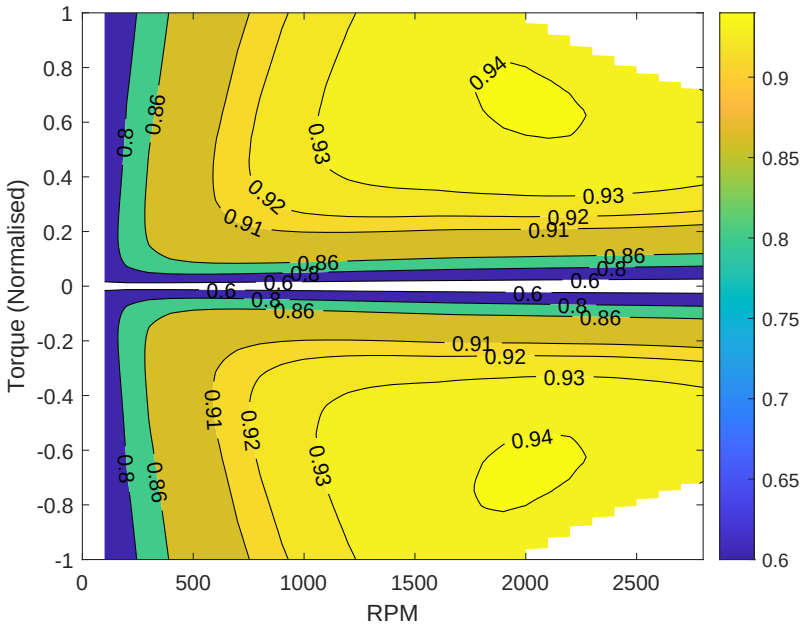

Figure 2.1: EM efficiency map for all feasible torque and RPM pairs.

The EM gearbox has 12 gears and the transmission losses are assumed constant in this thesis. The wheel rotation speed ω_w is related to the EM rotation speed ω_{EM} by

$$\omega_w = \frac{\omega_{EM}}{r_{EM}(\gamma) r_{tm}} \tag{2.7}$$

If zero slip is assumed, i.e. the rotation speed of the wheels correspond exactly to the speed of the vehicle, the relationship between motor rotation speed and vehicle speed is

$$\omega_{EM} = \frac{r_{EM}(\gamma) r_{tm} v}{r_{eff}} \tag{2.8}$$

The relationship between EM power P_{EM}, torque τ_{EM} and rotation speed ω_{EM} is

$$P_{EM} = \omega_{EM} \tau_{EM} \tag{2.9}$$

By using this relation and Equations (2.6), (2.8), tractive effort can be expressed as

$$F_T = \eta_{EM}(\omega_{EM}(\gamma), \tau_{EM}) \frac{P_{EM}}{v} \tag{2.10}$$

This equation serves as a measure of the electric power the ESS needs to supply for some desired tractive effort. When the EM is operating as a generator, the efficiency η_{EM} appears on the left hand side of Equation (2.10) instead.

2.2.2 Proton-exchange membrane fuel cell

Proton-exchange membrane fuel cells convert chemical energy into electrical energy by transforming hydrogen and oxygen into water. The voltage of a single cell is low, around 0.8 volts [18], so several cells are typically put together into a stack to obtain practical output voltages. Of current technologies, PEMFC is one of the most

suited for automotive applications due to their high power density, low operating temperature, fast startup and high efficiency [19][20].

Structure

A single proton-exchange membrane fuel cell has a layered structure. The authors of [19] provide a detailed description of it, which is the foundation of this section. The centre of the cell is a solid polymer electrolyte membrane, which is permeable for protons, but not for the reactant gases. The membrane is also an electric insulator, which consequently hinders electrons from passing through it (despite being smaller than protons). A catalyst layer, often platinum, is attached to each side of the membrane. It is on the catalyst surface which the electrochemical reactions that produce electricity happen. Beyond the catalyst layer is the gas diffusion layer which feeds reactant gases evenly over the catalyst and provides an electrical connection to the anode or cathode. The aforementioned layers are sandwiched between bipolar plates, either anode or cathode, which provides structural support for the cell, houses gas-flow channels and transfers heat to the cooling system.

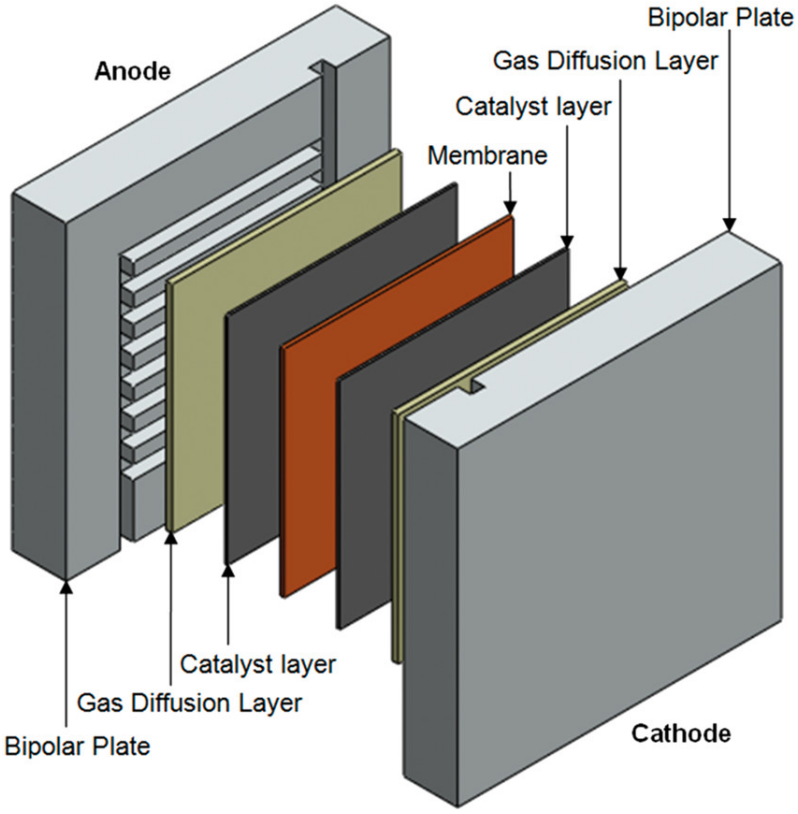

Figure 2.2: Illustration of PEMFC's layered structure [19].

Reaction

Hydrogen gas is fed through the gas flow channels and gas diffusion layer to the anode-side catalyst, where the electrochemical reaction is

$$H_2 \rightarrow 2H^+ + 2e^- \tag{2.11}$$

The resulting protons are fed through the membrane to the cathode side while the electrons pass through the electric circuit mentioned earlier to create an electric current. The reaction that occurs on the cathode side is,

$$\frac{1}{2}O_2 + 2H^+ + 2e^- \rightarrow H_2O \tag{2.12}$$

where the water produced is either in liquid or gas form. Refer to Figure 2.3 for an illustration of the process. The entire reaction in the cell is thus

$$H_2 + \frac{1}{2}O_2 \rightarrow H_2O \tag{2.13}$$

The fuel cell reaction is exothermic, meaning that energy is released in the process.

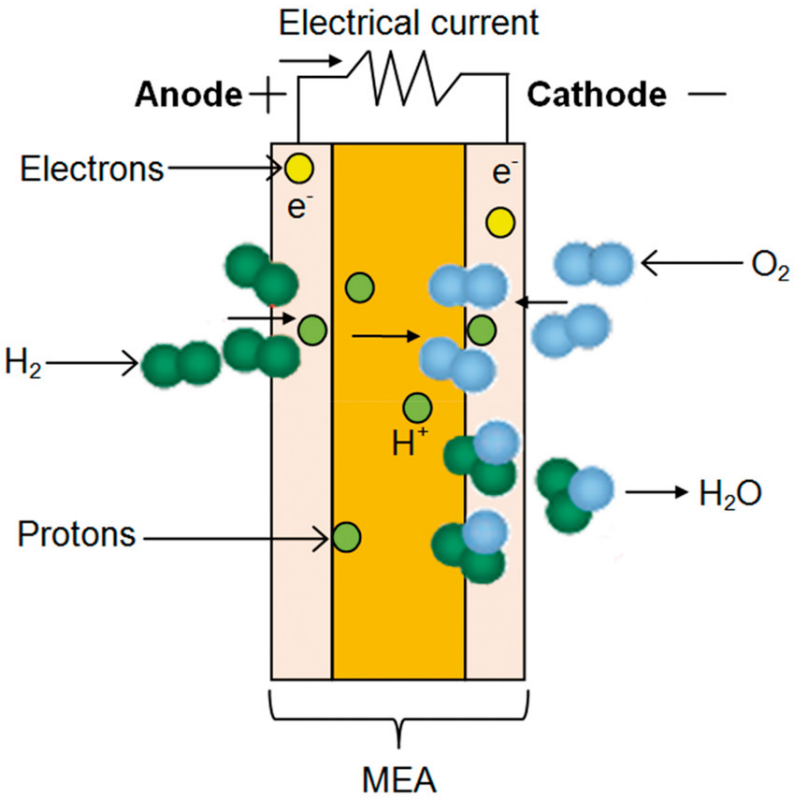

Figure 2.3: Illustration of the electrochemical reaction in PEMFC [19].

The reaction enthalpy ΔH is thus negative, which implies that the chemical bond energy of water is less than the energy of the reactants. The released energy is [21]

$$\begin{cases} H_2 + \frac{1}{2}O_2 \rightarrow H_2O \text{ (liquid)} & \Longrightarrow \quad \Delta H = -285.8 \text{ (kJ/mol)} \\ H_2 + \frac{1}{2}O_2 \rightarrow H_2O \text{ (gas)} & \Longrightarrow \quad \Delta H = -241.8 \text{ (kJ/mol)} \end{cases} \tag{2.14}$$

The value of $\Delta H = 285.8$ is known as hydrogen's higher heating value (HHV) and $\Delta H = 241.8$ is known as hydrogen's lower heating value (LHV). The difference in energy corresponds to the energy required to vaporise one mole of water from 25 $^\circ C$. The LHV is suitable for fuel cell calculations as the water is removed as vapour.

Operation

The fuel cell has hydrogen consumption and efficiency curves as seen in Figures 2.4a and 2.4b. The efficiency refers to the fraction of chemical energy (LHV) that is converted to electrical energy. The unutilised energy is lost through unreacted hydrogen and heat, where heat represents the majority of that energy [22]. Most of the heat is removed by the cooling system, but some is removed by the ambient air.

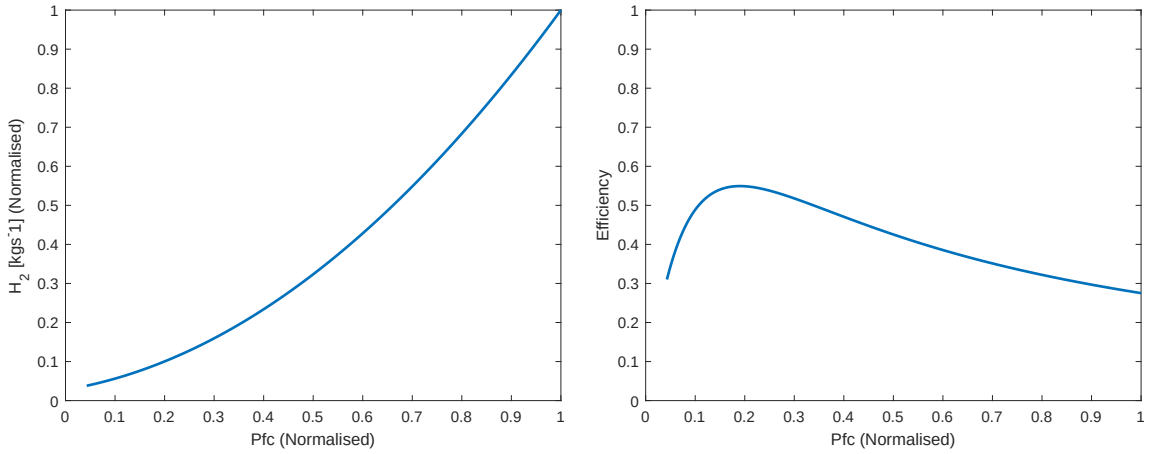

(a) **(b)**

Figure 2.4: **(a)**: Normalised hydrogen consumption as a function of normalised fuel cell power. **(b):** Fuel cell efficiency as a function of normalised fuel cell power.

It is seen in Figures 2.4a and 2.4b that the lowest 5% of fuel cell power P_{FC} is not used. This is to prevent catalyst degradation, which happens at very low loads due to surface oxide production [23]. High and transient fuel cell loads should also be avoided as they may incur fuel starvation, which degrade both the catalyst layer and gas diffusion layer through carbon oxidation [5].

2.2.3 Lithium-titanite battery

The considered battery consists of lithium-titanium-oxide (LTO) cells which have longer cycle life and higher charge/discharge power capacity than conventional graphite-based cells. Disadvantages of the cell are lower inherent voltage and lower specific energy than graphite cells [24]. The battery is comprised of a number of LTO cells in series and parallel. The capacity of the battery pack C_b, measured in Ampere-hours, is determined by the number of cells in parallel. The open circuit voltage (OCV) U_{OC} is determined by the number of cells in series and depends on the battery pack temperature and state of charge (SoC). The OCV for the LTO battery is shown in Figure 2.5. The SoC dynamics are described by

$$\dot{SoC} = \frac{-P_B - P_{B,loss}}{C_b U_{OC}(SoC)} \tag{2.15}$$

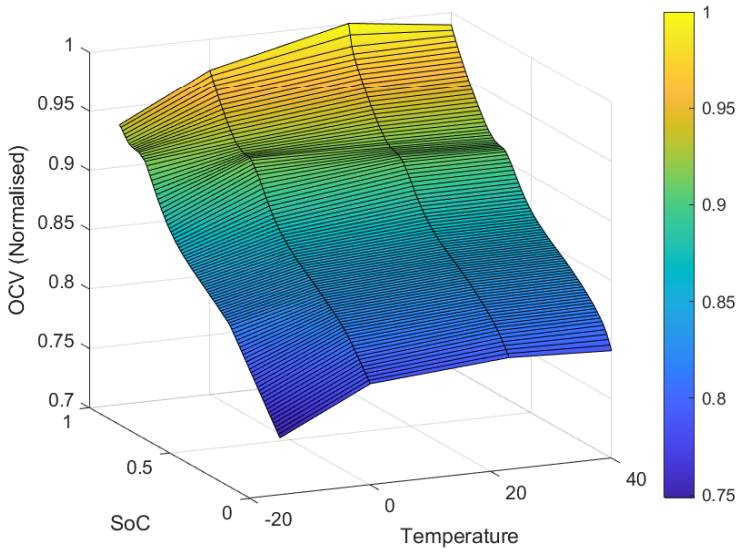

Figure 2.5: Battery OCV as a function of battery temperature and SoC.

where positive values of P_B discharge the battery. The amount of electric power that is lost as heat $P_{B,loss}$ is determined by the battery current and internal resistance. The resistive loss is typically taken as RI_B^2. The internal resistance varies with battery SoC and decreases with temperature, as seen in Figure 2.6.

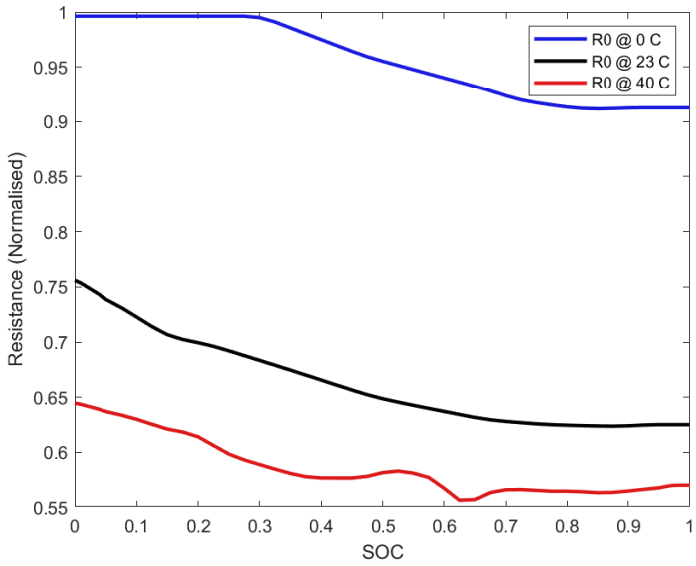

Figure 2.6: Battery internal resistance as a function of SoC for temperatures $0°, 23°$ and $40°$ C.

Even if the resistive loss decreases as temperature increases, it is ideal to operate LTO batteries around room-temperature. The authors of [25] show that commercial LTO cells reach end of life (defined as 80% remaining capacity) after only 1000 charge and discharge cycles at 55 $C°$. Although the specific cells used in the study

are undisclosed, several LTO-cell manufacturers claim cycle-lives above 10,000 cycles. This number is backed by a general summary on LTO-battery technology [24]. Furthermore, the internal resistance of the three cells used in [25] had increased between 50% and 300% by the end of life. In another article [26], it is shown that lithium-ion battery capacity and resistance degrade increasingly fast for temperatures above 25 $C°$. The authors of [27] also show through a post-mortem study that lithium-ion batteries degrade quickly during low-temperature operation. Furthermore, battery capacity and internal resistance degrade faster during high charge and discharge rates [28][29]. For this reason, automotive manufacturers limit the battery power. The limits used in this thesis are shown in Figure 2.7.

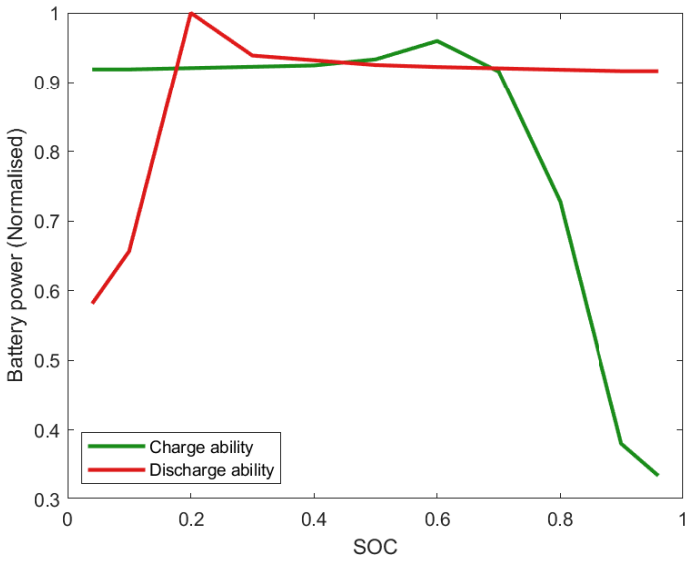

Figure 2.7: Maximum battery charge and discharge power as a function of battery SoC at 23° C.

3

Optimal control theory

This chapter provides the foundational theory for numerical nonlinear model predictive control. It does not attempt to fully explain the concepts, nor elaborate on all of the details as that discussion would be far too lengthy. For more information, please refer to [30][31][32].

3.1 Continuous-time optimal control

Most physical systems can be described by differential equations of the form

$$\dot{x}(t) = f(t, x(t), u(t)) \tag{3.1}$$

where t is time, x is the state vector and u is a vector of external inputs applied to the system. The external inputs are realised by some actuator and are henceforth referred to as control inputs. The state vector x contains *at least* the necessary information to fully describe the system's dynamics. The time dependency of the differential equation implies that the dynamics may be time variant.

Optimal control is concerned with finding the optimal state $x^*(t)$ and optimal control $u^*(t)$ of a system with respect to some objective function J. The objective function is traditionally minimised and is also referred to as a cost, or loss, function. The system's actuators typically have limited regions of operation, so a control constraint set $\mathcal{U}$, which $u^*(t)$ must belong to, is introduced. A state constraint set $\mathcal{X}$, which $x^*(t)$ must belong to, is introduced for similar reasons. The sets $\mathcal{U}$ and $\mathcal{X}$ may vary over time, but the current notation is kept for convenience. An initial state constraint $\mathcal{X}_0$, represents the initial configuration of the system. The initial state is typically predetermined by the application, in which case $\mathcal{X}_0$ is an equality constraint, but there are cases where $x^*(0)$ is found through optimisation. A considerable benefit of constrained optimal control is the ability to enforce a certain system state at the end of some time-horizon of interest $[0, T]$. For this reason, a final time constraint $\mathcal{X}f$ is introduced, which $x(T)$ must belong to. Sometimes, a combination, or function, of the state and control input need to be constrained. These functions can typically be described by a general inequality constraint of the form $g(t, x(t), u(t)) \leq 0$. With these constraint sets introduced, we are ready to present the continuous-time optimal control problem

$$J = \min_{x,u} \int_0^T l(t, x(t), u(t))\, dt \tag{3.2a}$$

subject to

$$\dot{x}(t) = f(t, x(t), u(t)) \tag{3.2b}$$

$$x(0) \in \mathcal{X}_0 \tag{3.2c}$$

$$x(t) \in \mathcal{X} \tag{3.2d}$$

$$x(T) \in \mathcal{X}_f \tag{3.2e}$$

$$u(t) \in \mathcal{U} \tag{3.2f}$$

$$g(t, x, u) \leq 0 \tag{3.2g}$$

The continuous optimal control problem, however, serves only as a theoretical method as there are infinite decision variables and constraints in the time span $[0, T]$. The problem must thus be divided into a finite number of discrete intervals N to be solved[1]. After discretisation, the continuous objective function, dynamics and constraints need only be evaluated at the indices $k \in [0, 1, ..., N-1, N]$. The state at some discrete time index t_{k+1} is obtained numerically through an initial-value problem (IVP)

$$x(t_k) = x_k, \quad \dot{x} = f(t, x(t), u(t)), \quad \text{for} \quad t \in [t_k, t_{k+1}] \tag{3.3}$$

It is assumed in this thesis that u is piece-wise constant, that is

$$u(t) = u(t_k), \quad \forall\, t \in [t_k, t_{k+1}) \tag{3.4}$$

Numerical integration

Numerical integration methods provide approximate solutions to IVPs such as those stated in Equation 3.3. The annotation $h_k = t_{k+1} - t_k$ is introduced as the discretisation steps may be non-equidistant. The integration method used in this thesis is the first order explicit Runge-Kutta method, often referred to as the explicit Euler method.

Explicit Euler method

The explicit Euler method is simple and easy to implement. It approximates the state at the next time-step through the update rule

$$x(t_{k+1}) = F(t_k, x(t_k), u(t_k), h_k) \tag{3.5}$$

where

$$F(t_k, x(t_k), u(t_k), h_k) = x(t_k) + h_k \cdot f(t_k, x(t_k), u(t_k)) \tag{3.6}$$

In each IVP, the explicit Euler method introduces a local integration error $\|\tilde{x}(t_{k+1}) - x(t_{k+1})\|$ of order $\mathcal{O}(h_k^2)$, i.e. it is proportional to the square of the discretisation step. The global integration error $\|\tilde{x}(T) - x(T)\|$ introduced by the method is $\mathcal{O}(h)$, if all time-steps are equidistant. For this reason, the explicit Euler method is referred to as a first-order integration method, which consequently requires very small step-sizes $h_k << 1$ to get moderate accuracy [30].

[1] Discretisation steps may be non-equidistant.

3.2 Nonlinear model predictive control

The NMPC problem is concerned with finding the optimal state and control sequence over the horizon $[0, T]$ for the system in Equation 3.1 at the discrete time indices $k \in [0, 1, ..., N-1, N]$. The system state at time t_{k+1} is obtained through the numerical solution to the IVP stated in Equation 3.3. The continuous optimal control problem introduced in Section 3.1 is now restated as a discrete-time optimal control problem

$$J = \min_{x,u} \sum_{k=0}^{N-1} l(t_k, x(t_k), u(t_k)) \tag{3.7a}$$

subject to

$$x(t_{k+1}) = F(t_k, x(t_k), u(t_k), h_k) \tag{3.7b}$$

$$x(0) \in \mathcal{X}_0 \tag{3.7c}$$

$$x(t_k) \in \mathcal{X} \tag{3.7d}$$

$$x(t_N) \in \mathcal{X}_T \tag{3.7e}$$

$$u(t_k) \in \mathcal{U} \tag{3.7f}$$

$$g(t_k, x(t_k), u(t_k)) \leq 0 \tag{3.7g}$$

The objective function is commonly used to track some reference, but in this thesis it is used to optimise the economic performance of system. This is known as Economic MPC. Several stability and performance-aspects of Economic MPC are found in [30]. Another aspect, which has not been discussed yet, is the inclusion of discrete actuators such as on/off switches or gearboxes. Rawlings et al. [30] state that the viability of the MPC formulation is retained in the presence of integer decision variables, but ask if it is practical to solve the mixed-integer MPC problem in the available sample time. The question remains unanswered, but it is hinted that optimisation solvers are addressing the computational problems. To the authors' knowledge, it is preferable to avoid mixed-integer formulations to keep computation cost down. At least in the current state of mixed-integer solvers.

3.3 Nonlinear optimisation

Once the discrete optimisation problem is formulated, it needs to to be solved. For this purpose, a nonlinear program (NLP) is formulated using the numerical solver FORCES PRO [33][34]. Assume that the NMPC problem formulated in Equation 3.7 is written on the form

$$\begin{aligned} \min_{z} \quad & f(z) \\ \text{subject to} \quad & h_i(z) = 0, \qquad i = 1, ..., p \\ & g_j(z) \leq 0, \qquad j = 1, ..., m \end{aligned} \tag{3.8}$$

where $z = \{z_1, ..., z_n\}$ are the optimisation variables, $h(z) = \{h_1(z), ..., h_p(z)\}$ are the equality constraints and $g(z) = \{g_1(z), ..., g_m(z)\}$ are the inequality constraints.

The optimal solution z^* is the z which yields the lowest cost $f(z)$ and belongs to the feasible set

$$\mathcal{S} = \{z \mid h_i(z) = 0, g_i(z) \leq 0, \forall i\} \tag{3.9}$$

Finding z^* is often trivial for linear or convex quadratic functions as the optimal solution is unique. Nonlinear functions, however, can have several local minima z^*, which are optimal solutions in a neighbourhood of z^*. Local minima have the property that for any step length ϵ and feasible direction d ($z^* + \epsilon d \in \mathcal{S}$), the cost $f(z^* + \epsilon d)$ is higher than $f(z^*)$.

Many optimisation algorithms utilise the mathematical properties of local minima to find the optimal solution z^* [30]. In the unconstrained case, the conditions for local optimality are

$$\begin{aligned} &z^* \text{ is a stationary point} \implies \nabla f(z^*) = 0 \\ &z^* \text{ is a strict local minimum} \implies \nabla f(z^*) = 0,\ \nabla^2 f(z^*) \succ 0 \end{aligned} \tag{3.10}$$

The positive-definiteness condition on $\nabla^2 f$ implies that z^* is a *unique* local minimum, i.e. $f(z^*) < f(z^* + \epsilon d)$. In the constrained case, local optimality is instead defined by the Karush-Kuhn-Tucker (KKT) conditions

$$\begin{aligned} &\nabla_z f(z^*) + \nabla_z g(z^*)\mu^* + \nabla_z h(z^*)\lambda^* = 0 \\ &h(z^*) = 0 \\ &g(z^*) \leq 0 \\ &\mu^* \geq 0 \\ &\mu_i^* g_i(z^*) = 0,\ i = 1, ..., m \end{aligned} \tag{3.11}$$

The first equation can be expressed as a condition on the Lagrangian

$$\nabla_z \mathcal{L}(z^*, \mu^*, \lambda^*) = 0, \qquad \mathcal{L}(z, \mu, \lambda) = f(z) + \mu^T g(z) + \lambda^T h(z) \tag{3.12}$$

where μ and λ are Lagrange multipliers, which are referred to as dual variables. The dual constraints $\mu^* \geq 0$ and $\mu_i^* g_i(z^*) = 0$ ensure that $\mu_i = 0$ if the inequality constraint is weakly active $g_i(z^*) < 0$. If the inequality constraint is strictly active $g_i(z^*) = 0$, then μ_i is determined by the Lagrangian gradient constraint. To illustrate this, imagine a local minimum which is blocked by an inequality constraint $g_i(z^*) \leq 0$. For $\nabla_z h(z^*)\lambda = 0$, μ^* is given explicitly by $\nabla_z f(z^*) + \nabla_z g(z^*)\mu^* = 0$. The result is an artificial equilibrium, much like the second condition in Equation 3.10, which enforces the inequality constraint $g(z^*) \leq 0$.

Interior point optimisation

Nonlinear interior point (IP) methods formulate a smooth approximation of the original problem. Equality-constrained optimisation problems are inherently smooth, but inequality-constrained problems contain the complementary conditions $\mu^* \geq 0$ and $\mu^* g_i(z^*) = 0$ which are not [30]. To address this, the inequality constraints $g_i(z) \leq 0$ are converted to equality constraints $g_i(z) + s_i = 0$ by introducing a slack variable $s \geq 0$. The inequality constraint $s \geq 0$ is then removed by adding a barrier

term $-\tau \sum_{i=1}^{m} \log(s_i)$ which grows to infinity as $s \to 0$. The optimisation problem can then be reformulated as

$$\begin{aligned} \min_{z,s} \quad & f(z) - \tau \sum_{i=1}^{m} \log(s_i) \\ \text{subject to} \quad & h_i(z) = 0, \qquad i = 1, ..., p \\ & g_i(z) + s = 0, \qquad i = 1, ..., m \end{aligned} \tag{3.13}$$

It can be shown that the barrier function is a perfect indicator of the feasible set $\mathcal{S}$ as $\tau \to 0$ [30]. For any $\tau > 0$, the KKT conditions are a smooth set of equations which can be formulated as

$$\begin{aligned} & \nabla_z \mathcal{L}(z, \mu, \lambda) = 0 \\ & h_i(z) = 0 \\ & g_i(z) + s = 0 \\ & \mu_i s_i = \tau, \; i = 1, ..., m \end{aligned} \tag{3.14}$$

A smooth problem can be solved through iterative root-finding methods such as Newton's method or its variants. Nonlinear IP methods utilise these and solves the problem by first setting the barrier term τ to a fairly large value. The value of τ is then decreased and solved again, using the previous solution to initialise the problem. The final solution is an approximation of the true optimum as a numerical method with finitely many steps is used. For nonlinear and non-convex problems, the root-finding method may diverge or fail to find the global solution. To illustrate this, we will look at the unconstrained fourth order polynomial function $f(z)$ shown in Figure 3.1a. The green marker indicates the global optimum, the red a local maximum and the blue a local minimum. A Newton method takes an initial guess and iterates

$$z^+ = z - (\nabla_z^2 f(z))^{-1} \nabla f(z) \tag{3.15}$$

until some tolerance on $\|z^+ - z\|$ has been met. Figure 3.1b and 3.1c show the Jacobian and Hessian of $f(z)$ respectively. The Newton method follows the tangent of $\nabla f(z)$ to a nearby stationary point. For this reason, the found stationary point depends on the provided initial guess. Figure 3.1b shows three initial guess regions, from which an initial guess will converge to the stationary point with the same colour in Figure 3.1a. The Newton method fails if $\nabla^2 f(z)$ is zero as the hessian of $f(z)$ is inverted. Figure 3.1c shows that this is the case for two values of z in the example function.

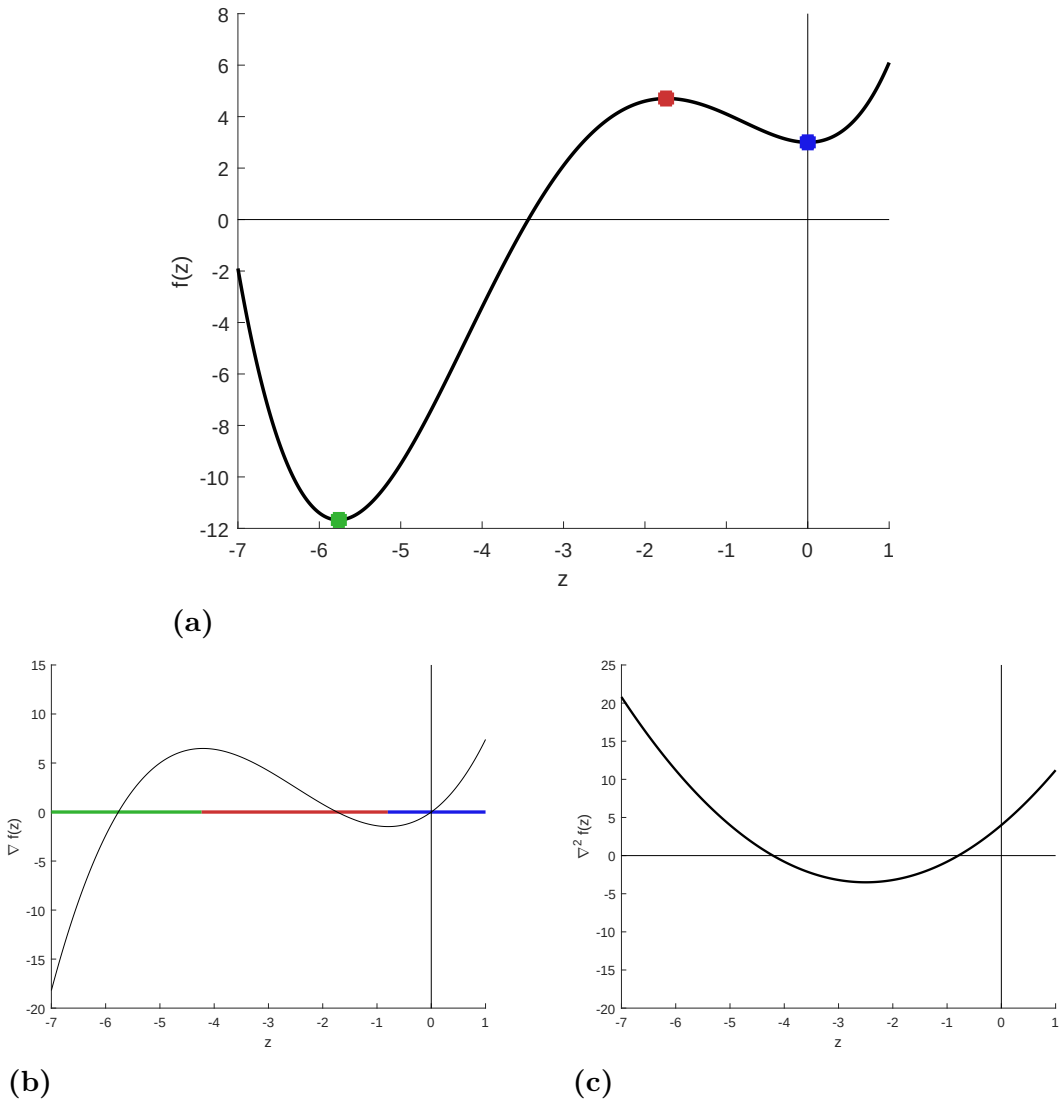

(a) **(b)** **(c)**

Figure 3.1: **(a):** Function to minimise **(b):** Its Jacobian **(c):** Its Hessian for $z \in [-7, 1]$. **(b):** The green, red and blue x-axis colours indicate to which stationary point in **(a)** the classic Newton method converges to.

4

Optimisation model

In this chapter, the vehicle model is augmented to make it suited for numerical solution by an nonlinear IP method. As was stated in chapter 3, the problem should be smooth and preferably quadratic, or at least convex within the system constraints.

4.1 Electric motor

In a vehicle, there is typically more than one gear that enables some desired traction effort at a given vehicle speed. This can also be seen in Equation 2.8, which is restated here for convenience.

$$\omega_{EM} = \frac{r_{EM}(\gamma) r_{tm} v}{r_{eff}} \tag{4.1}$$

Low-level controllers have to make a gear decision, e.g. through mixed-integer optimisation. As the controller developed in this thesis does not control the vehicle directly, the integer decision is preferably omitted. This is achieved by assuming that a low-level controller is consistently choosing the efficiency-optimal gear. Under this assumption, a gear map is constructed for all feasible vehicle speed and traction effort pairs, shown in Figure 4.1a. The related efficiency map is shown in Figure 4.1b.

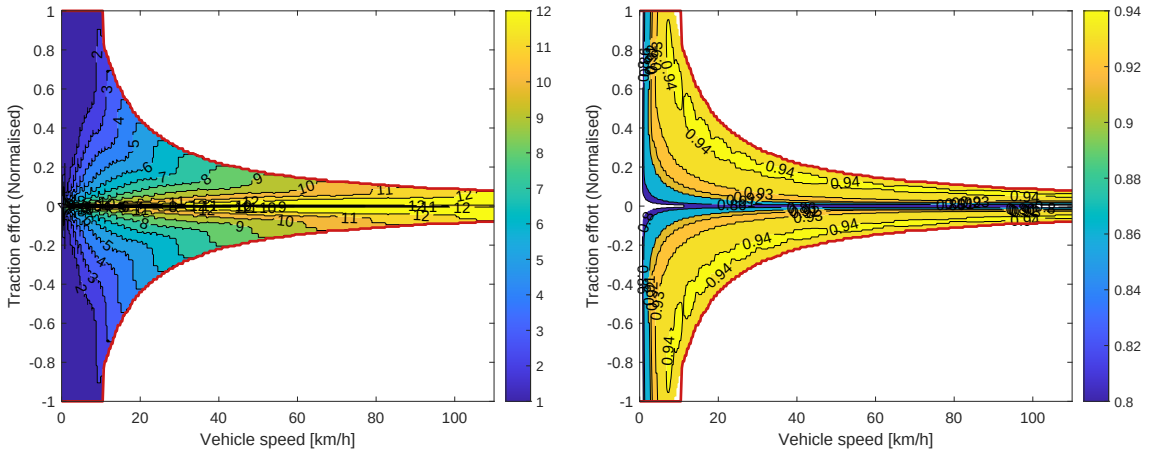

(a) **(b)**

Figure 4.1: **(a)**: Optimal gear map and speed-dependent traction effort bounds (red). **(b):** EM efficiency at optimal gear and speed-dependent traction effort bounds (red).

As the EM efficiency $\eta_{EM} = 0.93$ dominates the typical operation regions, it is used as a constant instead of using the full map. The efficiency falls much lower close to zero traction effort, but the modelling mismatch is deemed irrelevant as the energy loss is negligible when $F_T \to 0$. Through this abstraction, traction effort is decoupled from the gears and can be expressed as

$$F_T = \eta_{EM} \frac{P_{EM}}{v} \tag{4.2}$$

The traction effort bounds, shown in red in Figures 4.1a and 4.1b, are smooth functions used as inequality constraints in the optimisation.

4.2 Power split

The fuel cell and battery provide power to the DC Bus, which splits it to the EM, cooling system and auxiliary loads. The battery can be charged through regenerative breaking or directly by the fuel cell. The power from the fuel cell used to charge the battery is denoted by $P_{FC \to B}$. An efficiency $\eta_{DC} = 0.99$ is assumed in the transfer. The battery cannot be charged and discharged at the same time. The power flow during propulsion and regenerative breaking is illustrated in Figure 4.2a and Figure 4.2b respectively. During battery discharge, the power to the EM is

$$P_{EM} = \max(0, P_{FC} + P_B - P_C - P_{aux}) \tag{4.3}$$

where the max function is used to emphasise that power is taken from P_{FC} and P_B to the cooling system and auxiliary loads, i.e. P_C and P_{aux} cannot make P_{EM} negative. By using Equation 4.2, the traction effort at the wheels is

$$F_T = \eta_{EM} \frac{\max(0, P_{FC} + P_B - P_C - P_{aux})}{v} \tag{4.4}$$

During regenerative breaking, there is no power from the fuel cell to the EM and no power from the battery to the cooling system or auxiliary loads. Thus, the power taken from the EM is $P_{EM} = P_B$. The efficiency factor $\eta_{EM} = 0.93$ in Equation 4.2 holds for propulsion, but power flows in the opposite direction during regenerative breaking so it enters the equation on the left hand side instead, i.e. $\eta_{EM} F_T = \frac{P_{EM}}{v}$. The traction effort during recuperation is thus

$$F_T = \eta_{reg} \frac{P_B}{v} \tag{4.5}$$

where $\eta_{reg} = \frac{1}{\eta_{EM}}$ and $P_B < 0$. To separate the efficiencies for positive and negative

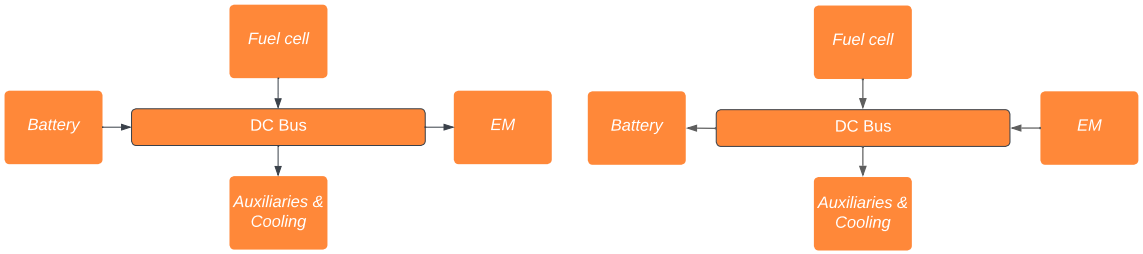

(a) **(b)**

Figure 4.2: **(a)**: Power flow during battery discharge. **(b)**: Power flow during regenerative breaking.

battery power, a new variable $P_{B,reg}$ is introduced. The variables P_B and $P_{B,reg}$ are nonnegative. Traction effort during regenerative breaking is then expressed as

$$F_T = -\eta_{reg} \frac{P_{B,reg}}{v} \tag{4.6}$$

It is desirable to formulate the traction effort equation without using the max function as it is inherently non-smooth. The formulation should also allow either of the fuel cell and battery to supply power to the cooling system and auxiliary loads. This is done as

$$F_T = \frac{\eta_{EM}(P_{FC} + P_B - P_C - P_{aux}) - \eta_{reg} P_{B,reg}}{v} \tag{4.7}$$

The max-function removal implies that P_C and P_{aux} are used for breaking if $P_{FC} + P_B < P_C + P_{aux}$. This is of course unrealistic, but the effect is nearly negligible as we shall see. The energy-optimal solution during breaking is to let $P_C + P_{aux}$ retard the vehicle and use $P_{FC \to B}$ to charge the battery. The energy transfer efficiency is thus $\eta_{DC} = 0.99$ instead of $\eta_{reg} = 0.93$ for the breaking power $P_C + P_{aux}$. The cooling and auxiliary powers are, however, typically very small compared to $P_{B,reg}$ during recuperation. The modelling inaccuracy is therefore accepted as the model is otherwise simple and effective. The condition that the battery cannot be charged and discharged at the same time is enforced by the constraint

$$P_B P_{FC \to B} = 0 \tag{4.8}$$

For an energy-optimal controller. There is actually no need to constrain $P_B P_{B,reg} = 0$ as accelerating and breaking simultaneously would present losses. Nevertheless, the constraint is still present.

4.3 Battery

For a mission planner, a model which accurately predicts future battery SoC is of interest. The model should also consider SoC-dependent charge and discharge limits to suggest feasible control actions. The SoC dynamics presented in Chapter 2,expressed through the variables introduced in the previous section, are

$$\dot{SoC} = \frac{\eta_{DC} P_{FC\to B} + P_{B,reg} - P_B - P_{B,loss}}{C_b U_{OC}(SoC)} \tag{4.9}$$

where a linear fit of $U_{OC}(SoC)$ is made at $T_B = 23C^\circ$ as thermal control systems maintain that temperature. The battery resistive losses are estimated through the simple internal resistance model shown in Figure 4.3. Its governing equation is

$$U_{OC}(SoC) = R(T_B, SoC)I_B + U_B \tag{4.10}$$

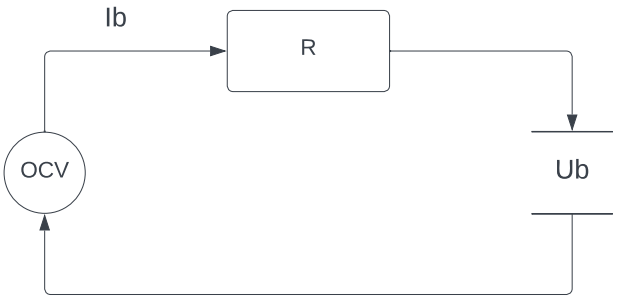

Figure 4.3: Internal resistance battery model.

The resistive loss is given by $R_B I_B^2$, so Equation 4.10 is multiplied by I_B which also yields an expression depending on P_B

$$U_{OC}(SoC)I_B = R(T_B, SoC)I_B^2 + P_B \tag{4.11}$$

This equation is rearranged to obtain a second-order root finding problem

$$I_B^2 \frac{U_{OC}(SoC)}{R(T_B, SoC)} I_B - P_B = 0 \tag{4.12}$$

The internal resistance depends on both battery temperature and SoC, but on-board control systems maintain the temperature $T_B \approx 23\ C^\circ$. For this reason a fit

$$P_{B,loss} = b_0 P_B^2 + b_1 SoC P_B^2 \tag{4.13}$$

is made assuming $T_B = 23\ C^\circ$. The fit, which is shown in Figure 4.4, closely resembles the resistive loss at $T_B = 23\ C^\circ$. The function is however not convex, but it can be made convex by removing the SoC-dependency at the loss of some modelling accuracy. As outlined above, negative values of P_B correspond to $P_{B,reg} + P_{FC\to B}$. It is assumed that 90% of the heat needs to be cooled, i.e. $\dot{Q}_B = 0.9 P_{B,loss}$.

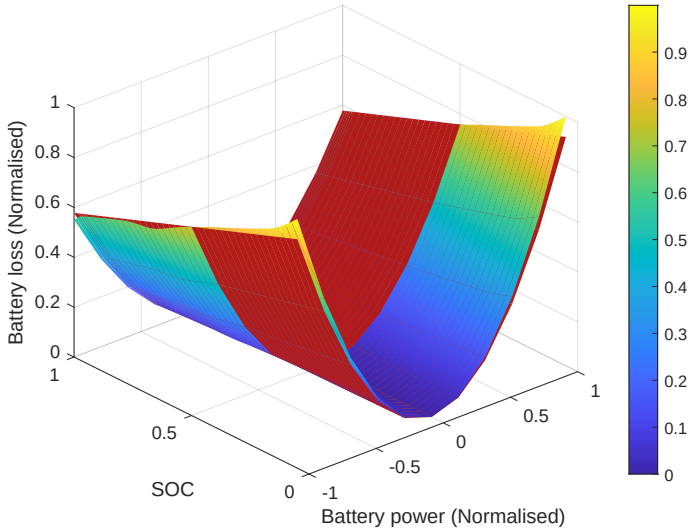

Figure 4.4: Resistive loss fit (red) and battery resistive loss at $T_B = 23\ C°$.

The SoC-dependent charge and discharge power limits are enforced by the smoothed nonlinear inequality constraints shown in Figure 4.5.

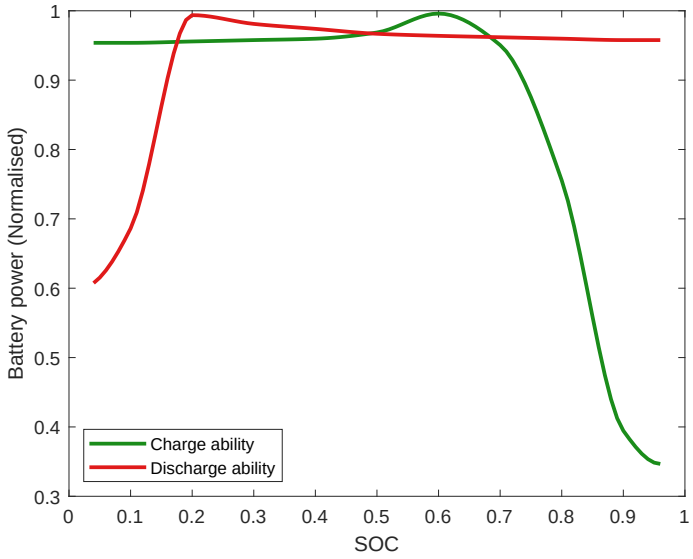

Figure 4.5: Smoothed battery charge and discharge power limits at $T_B = 23\ C°$.

4.4 Fuel cell

The hydrogen consumption is a second order polynomial function of the form

$$\dot{H}_{con} = a_0 + a_1 P_{FC} + a_2 P_{FC}^2 \tag{4.14}$$

The function is convex so it is suited for a nonlinear IP optimisation method. To retain the convexity, the hydrogen tank is considered full when $H_{con} = 0$. As mentioned in Chapter 2, most of the unutilised hydrogen energy is released as heat. The majority of that heat remove must be removed by the cooling system. Figure

4.6 shows the energy allocation assuming a fixed percentage of unreacted hydrogen and ambient heat dissipation. The heat which the cooling system needs to remove Q_{FC} is given by the convex second order function of the fuel cell power shown in Figure 4.7 and described by

$$\dot{Q}_{FC} = c_0 + c_1 P_{FC} + c_2 P_{FC}^2 \tag{4.15}$$

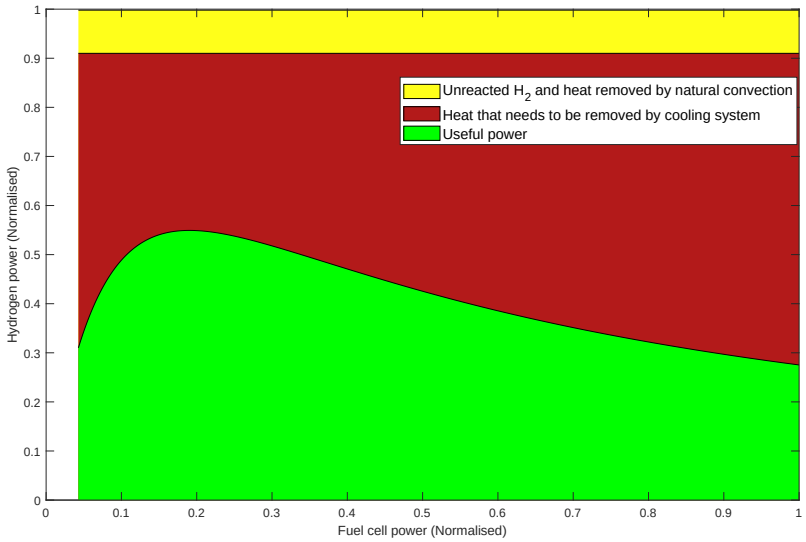

Figure 4.6: Fuel cell efficiency at different power outputs

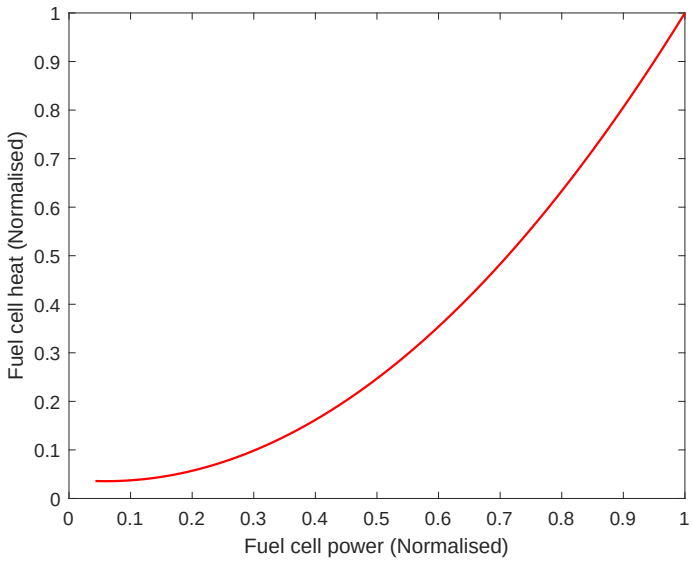

Figure 4.7: Heat generation from fuel cell at different power outputs

4.5 Cooling system power demand

The cooling system of an electric vehicle is complex and the required electric power depends on the temperature of the powertrain components, ambient air and cooling

liquids. Including states and control inputs for all the relevant quantities would increase the problem-size to impractical proportions. To avoid this, it is assumed that the powertrain components are at their respective desired temperatures. In this scenario, on-board thermal control systems remove the heat generated in the powertrain components to maintain their temperature, so the heat to cool is known through $\dot{Q}_{FC}$ and $\dot{Q}_B$. Assuming the electric cooling power is linearly dependent on the generated heat yields a quadratic and convex function. As the temperature differs between the fuel cell and battery, the linear dependence is not the same. Electric power required for cooling is thus approximated as

$$P_C = d_{FC}\dot{Q}_{FC} + d_B\dot{Q}_B \tag{4.16}$$

where d_{FC} and d_B are constants relating the generated heat to electric power. Due to the reductive nature of the approximation, it is not accurate. However, accounting for the cooling power is important as the momentaneous power output and overall fuel consumption is otherwise too low.

4.6 Space sampling

The optimisation problem is greatly simplified by sampling in space instead of time as road characteristics and hydrogen stations become fixed on the MPC-horizon. For this purpose, the short-hand notation $x' = \frac{\partial x}{\partial s_p}$, where s_p is distance along the vehicle's path, is introduced. The state dynamics are then expressed in change per meter. Transforming the differential equation

$$\dot{x}(t) = f(t, x(t), u(t)) \tag{4.17}$$

to the spatial domain is trivial as

$$x' = \frac{\partial x}{\partial s_p} = \frac{\partial x}{\partial t}\frac{\partial t}{\partial s_p} = \frac{\dot{x}}{v} \tag{4.18}$$

The differential equation to optimise is thus

$$x'(s_p) = \frac{f(s_p, x(s_p), u(s_p))}{v(s_p)} \tag{4.19}$$

The differential equations stated previously in this chapter are divided by the vehicle speed to obtain

$$t' = \frac{1}{v} \tag{4.20}$$

$$\begin{aligned} v' = &\frac{1}{mv}\Big(\frac{\eta_{EM}(P_{FC} + P_B - P_C - P_{aux}) - \eta_{reg}P_{B,reg}}{v} - F_{break} \\ &- mg\left(C_{rr}cos(\alpha) + sin(\alpha)\right) - \frac{1}{2}\rho_{air}C_dA_{v,f}v^2\Big) \end{aligned} \tag{4.21}$$

$$H'_{con} = \frac{1}{v}(a_0 + a_1P_{FC} + a_2P_{FC}^2) \tag{4.22}$$

$$SoC' = \frac{\eta_{DC} P_{FC\to B} + P_{B,reg} - P_B - P_{B,loss}}{v C_b U_{OC}(SoC)} \tag{4.23}$$

The conversion to space sampling increases the complexity of the state dynamics, especially for vehicle speed. This can be partly mitigated by transforming certain states and inputs. The state v is exchanged for a mass-normalised energy state

$$E = \frac{v^2}{2} \implies E' = v\frac{\partial v}{\partial s_p} = v\frac{\partial v}{\partial t}\frac{\partial t}{\partial s_p} = \dot{v} \tag{4.24}$$

The power control inputs are replaced by fictional forces

$$F_{FC} = \frac{P_{FC}}{v} \tag{4.25}$$

$$F_B = \frac{P_B}{v} \tag{4.26}$$

$$F_{B,reg} = \frac{P_{B,reg}}{v} \tag{4.27}$$

$$F_{FC\to B} = \frac{P_{FC\to B}}{v} \tag{4.28}$$

Expressed in the transformed states and inputs, the dynamics are

$$t' = \frac{1}{\sqrt{E}} \tag{4.29}$$

$$\begin{aligned} E' =& \frac{1}{m}\Big(\eta_{EM}(F_{FC} + F_B - F_C - \frac{P_{aux}}{\sqrt{E}}) - \eta_{reg} F_{B,reg} - F_{break} \\ & - mg\left(C_{rr} cos(\alpha) + sin(\alpha)\right) - \rho_{air} C_d A_{v,f} E\Big) \end{aligned} \tag{4.30}$$

$$H'_{con} = \frac{a_0}{\sqrt{E}} + a_1 F_{FC} + a_2\sqrt{2E} F_{FC}^2 \tag{4.31}$$

$$SoC' = \frac{\eta_{DC} F_{FC\to B} + F_{B,reg} - F_B - F_{B,loss}}{C_b U_{OC}(SoC)} \tag{4.32}$$

where F_C is the cooling system power demand expressed in the transformed inputs

$$F_C = d_{FC}(\frac{c_0}{\sqrt{E}} + c_1 F_{FC} + c_2\sqrt{E} F_{FC}^2) + d_B(b_0\sqrt{E} F_B^2 + b_1 SoC\sqrt{E} F_B^2) \tag{4.33}$$

4.7 Refuelling

The hydrogen consumption dynamics are extended to accommodate refuelling as

$$H'_{con} = \left(\frac{a_0}{\sqrt{2E}} + a_1 F_{FC} + a_2\sqrt{2E}\, F_{FC}^2\right) - s\frac{s_f}{\sqrt{2E}} S_g(E) \tag{4.34}$$

where $s \in \{0, 1\}$ is a parameter denoting fuel station existence at the current position, s_f is the station hydrogen fuelling speed and $S_g(E)$ is a sigmoid function given by

$$S_g(E) = \frac{1}{1 + e^{8\sqrt{2E} - 50}} \tag{4.35}$$

which enables the refuelling dynamics at low speeds. The function is shown for vehicle speeds $v \in [0, 80]$ kilometres per hour in Figure 4.8. The function is a smooth approximation of an on/off decision (which has an infinite derivative). The transition region cannot be too step as high derivative values may cause solver instability, but it should also be small enough to avoid decisions between on and off.

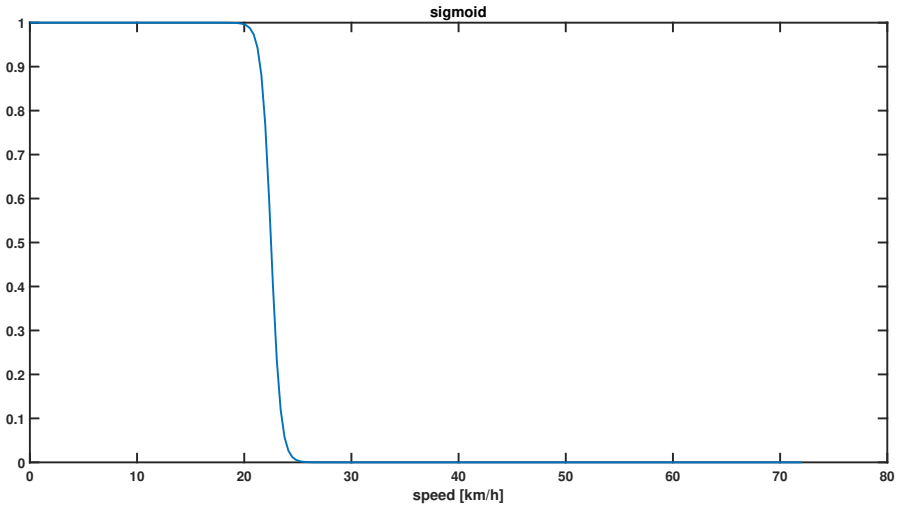

Figure 4.8: Sigmoid function $S_g(E)$

The purpose of $S_g(E)$ is to avoid fuel gain when the truck is passing stations at high speeds. The amount of fuel gained depends on the time spent in the sample, which is directly related to the vehicle speed. It should also be noted that the road discretisation step determines the maximum fuel gained, so it must be sufficiently long for the method to be viable. Hydrogen station queue time is incorporated in the optimisation formulation by the sigmoid function as well. When fuel is gained, the time state is increased by the station queue time t_q as

$$t' = \frac{1}{\sqrt{2E}} + S_g(E)t_q \tag{4.36}$$

Note that $S_g(E)t_q$ is not integrated over in the time state update.

4.8 Objective function

The objective function for the optimisation problem is defined as

$$J_1(\cdot) = \sum_{k=1, k\neq s_i}^{N} c_\delta \delta(k) + c_{H2}\left(H_{con}(k) - H_{con}(k-1)\right) + c_t\left(t(k) - t(k-1)\right) + c_b F_{break}(k) \tag{4.37}$$

Where the cost parameters c_δ, c_{H2}, c_t and c_b are normalised in terms of Swedish crowns and s_i denotes index where a fuelling station is present. At station samples where H_{con} is reduced, the associated cost term will become negative. Therefore a

separate function is introduced at samples where stations are present.

$$J_2(\cdot) = \sum_{k=s_0}^{s_N} c_\delta \delta(k) + c_{stat} \left(H_{con}(k-1) - H_{con}(k)\right) S_g(E(k)) \\ + c_t \left(t(k) - t(k-1)\right) + c_f S_g(E(k)) \quad (4.38)$$

Where s_0 and s_N denote the indices of the first and last fuelling station respectively, c_{stat} is the station specific fuel cost and c_f is the cost for stopping at a station. The function $J_2(\cdot)$ is thus, summed over the indices where stations are present. The objective function to minimise is then $J_1 + J_2$. A full formulation of the NMPC problem is presented in Appendix A.1.

5
Mission planner evaluation

To evaluate the efficacy of the mission planner, it is evaluated against two predictive energy management (PEM) controllers. The first controller, henceforth referred to as "simple-PEM", uses the road speed limit as an input and splits the power outputs between the fuel cell and the battery, while having a SoC reference of 50% during the driving cycle. The second PEM controller, henceforth referred to as "Planned-PEM", uses the SoC trajectory and refuelling plan from the mission planner as reference targets for the driving cycle. The prediction horizon for the PEM controllers is set to $\sim 3\ km$. All controllers and test cases use the same power train structure. For a full problem description of the PEM-controllers see A.2. All station specific parameters are assumed based on values from [35, 36].

Three cases are defined to evaluate different aspects of the mission planner,

- **Case 1:** A driving cycle with large hills, no refuelling stations and a time constraint
- **Case 2:** A driving cycle with frequent hills, refuelling stations and a time constraint.
- **Case 3:** A driving cycle with large hills, refuelling stations and no time constraint.

For Case 1, the planner operates under a time constraint which is set by the time the simple-PEM controller takes to complete the trip. The planner has a terminal SoC constraint which is also set by the terminal SoC of the simple-PEM controller.

In Case 2, refuelling stations are added. The simple-PEM controller is manually set to fuel at the first available station. The amount of fuel left at the end of the trip for the PEM controller is set as a terminal constraint for the mission planner. This is to make a fairer comparison in trip price. The station specific parameters in this case are presented in Table 5.1.

Table 5.1: Table of station specific parameters for case 2

station position [km]	Station fuelling speed [kg/s]	Station fuel price [SEK/kg]	Station queue time [minutes]
51	0.04	130	20
109	0.06	110	0
135	0.08	110	15
336	0.08	110	15
437	0.06	120	5

For case 3, it is of interest to see what happens when the planner has access to an infinite amount time and how this affects the mission. Here, results for the PEM controllers are of no interest. Station specific parameters for this case are presented in Table 5.1.

Table 5.2: Table of station specific parameters for case 3

station position [km]	Station fuelling speed [kg/s]	Station fuel price [SEK/kg]	Station queue time [minutes]
114	0.06	130	15
159	0.08	130	0
188	0.08	110	20
512	0.06	115	10

5.1 Case 1

This section outlines the result obtained when solving the problem formulation described in section 4.8, applied to Case 1 for the mission planner. The driving cycle is based on real-world measurements and is considered a challenging route for trucks. Figure 5.1 illustrates a comparison between the PEM controllers and mission planner for speed and SoC trajectories.

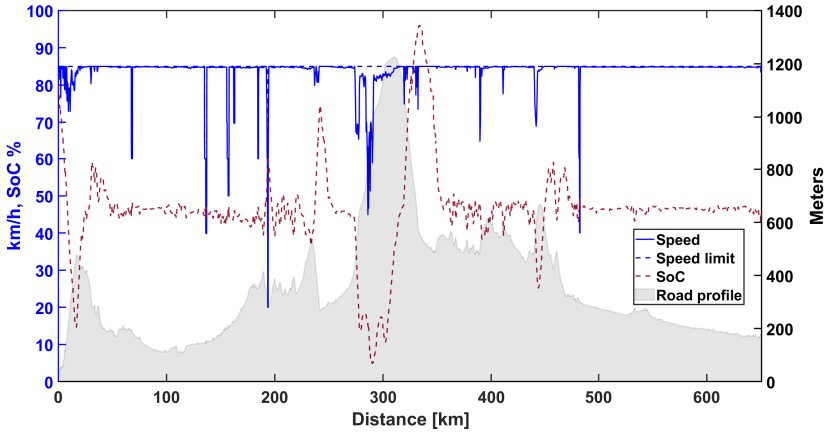

(a) Speed and SoC trajectory of the simple-PEM controller for a 40 ton truck

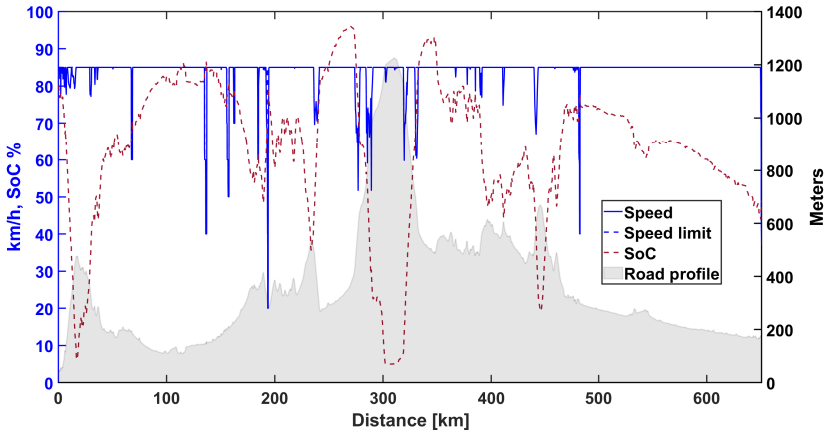

(b) Speed and SoC trajectory of the mission planner for a 40 ton truck

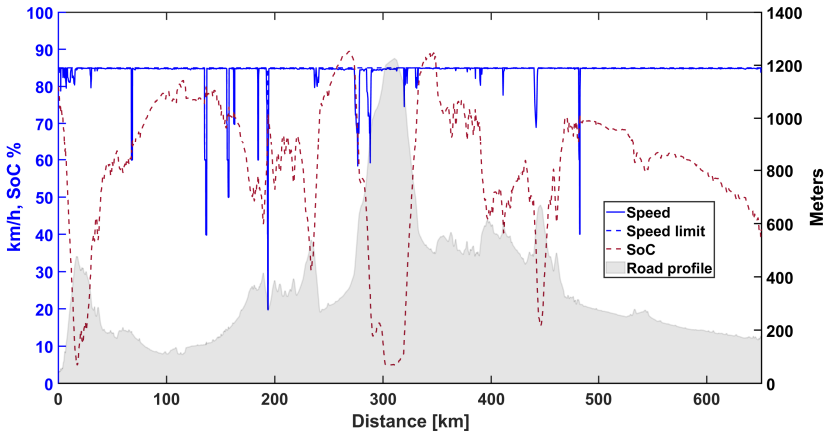

(c) Speed and SoC trajectory of the planned-PEM controller for a 40 ton truck

Figure 5.1: Speed and SoC comparison between the PEM controllers and the mission planner in case 1

Also, Figure 5.2 illustrates a comparison between the power split for the three controllers.

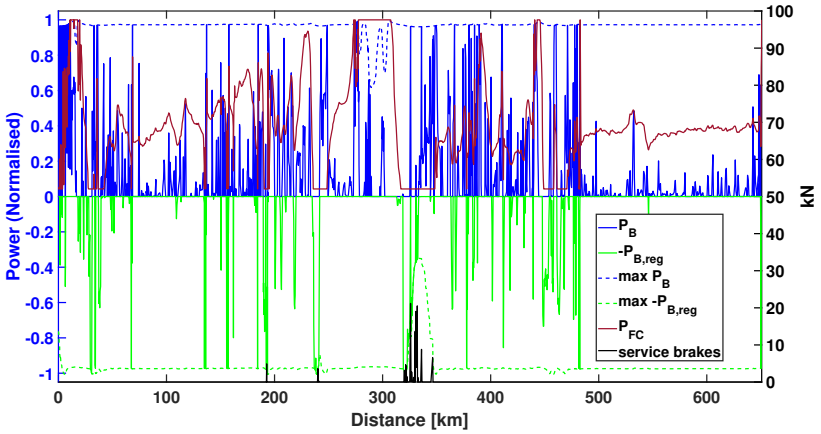

(a) Power split of the simple-PEM controller for a 40 ton truck

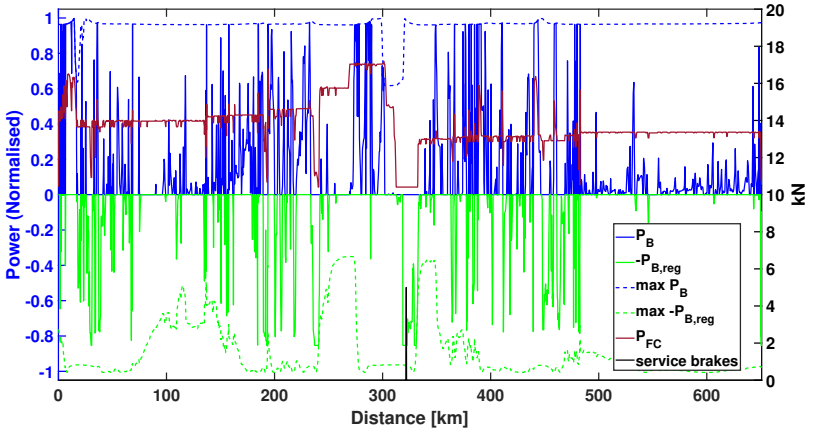

(b) Power split of the mission planner for a 40 ton truck

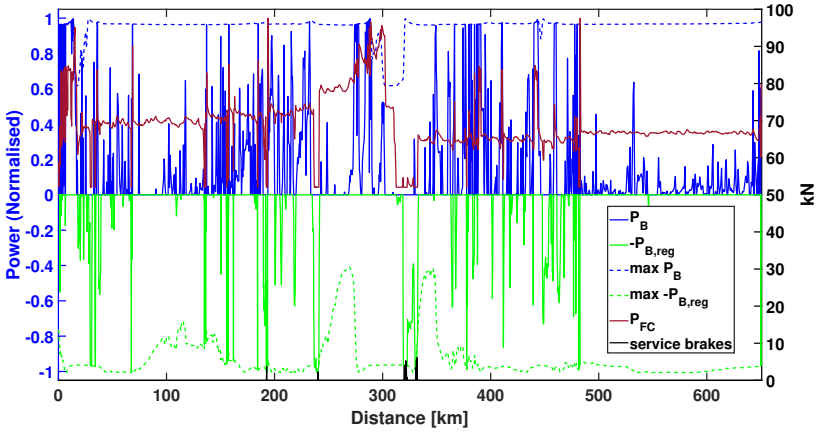

(c) Power split of the planned-PEM controller for a 40 ton truck

Figure 5.2: Power split comparison between the three controllers in case 1. P_B and $P_{B,reg}$ is the output- and regenerative braking power respectively. P_{FC} is the total power output from the fuel cell

Furthermore, Figure 5.3 illustrates a comparison in fuel cell usage of the three controllers with respect to fuel cell efficiency.

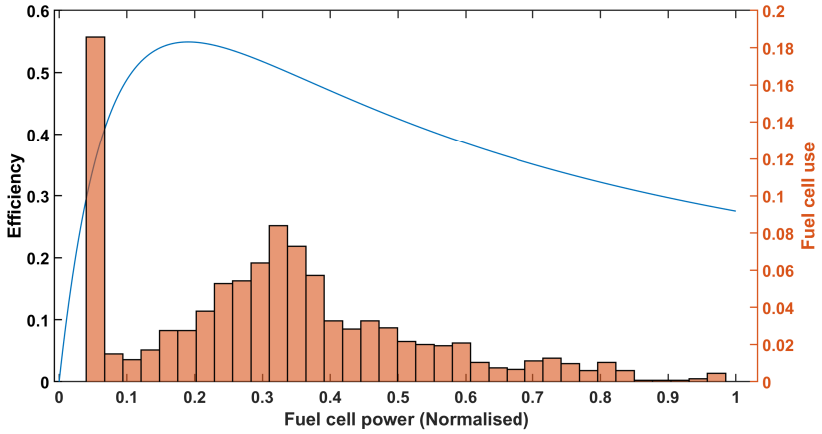

(a) Fuel cell usage of the simple-PEM controller for a 40 ton truck

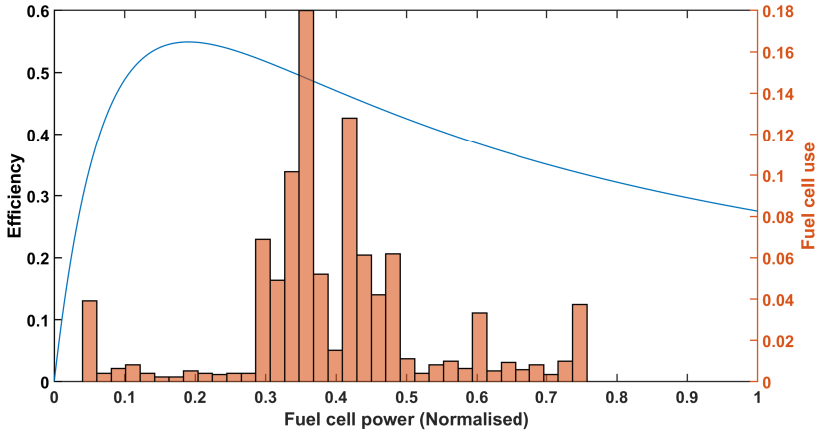

(b) Fuel cell usage of the mission planner for a 40 ton truck

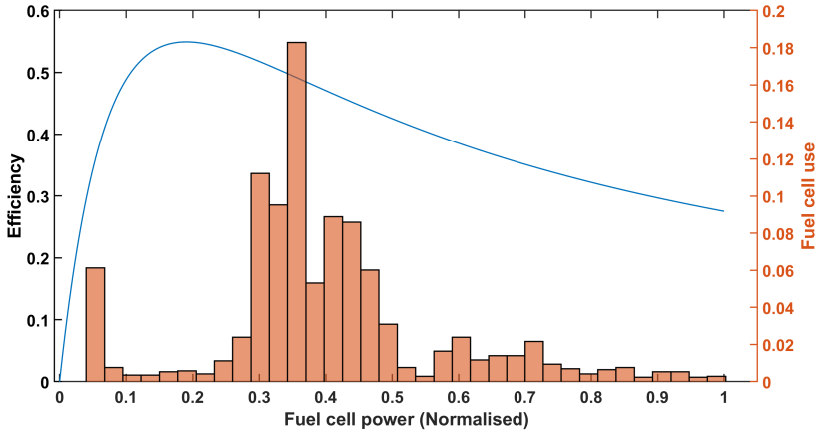

(c) Fuel cell usage of the planned-PEM controller for a 40 ton truck

Figure 5.3: Fuel cell usage comparison between the three controllers in case 1

Table 5.3 presents the results for the controllers. The energy consumption metric is normalised and set to 1 for the controller which consume the most energy.

Table 5.3: Summary of energy results in case 1

Controller	Energy consumption (normalised)	Trip time [h]	Average speed [km/h]	Initial SoC [%]	Final SoC [%]
Simple-PEM	1	7.79	82.5	80	46
Mission planner	0.85	7.79	82.5	80	50
planned-PEM	0.87	7.76	82.8	80	48

5.2 Case 2

This section outlines the result obtained when solving the problem formulation described in section 4.8, applied to Case 2 for the mission planner. The driving cycle is based on real-world measurements. The presence of hydrogen fuel stations exists, however, the position of the stations are assumed. Figure 5.4 illustrates a comparison between the PEM controllers and mission planner for speed and SoC trajectories, also included are refuelling decisions.

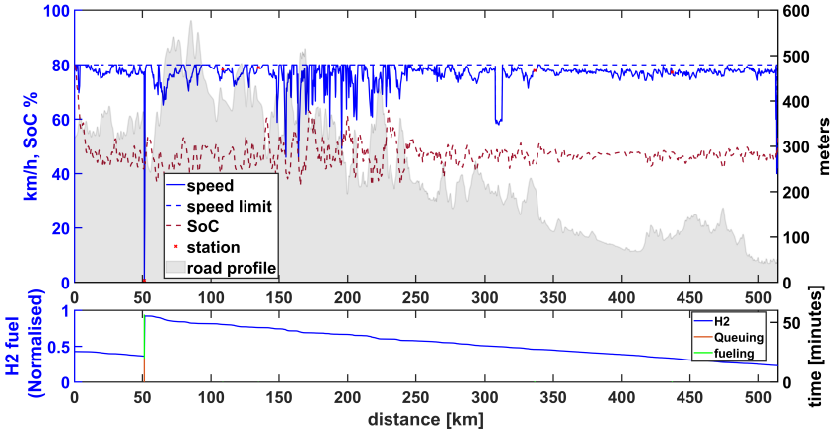

(a) Speed, SoC and fuel trajectories of the simple-PEM controller for a 40 ton truck

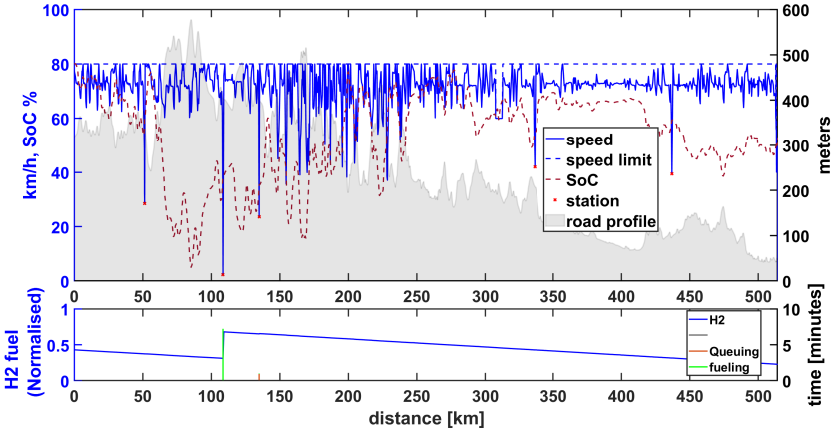

(b) Speed, SoC and fuel trajectories of the mission planner for a 40 ton truck

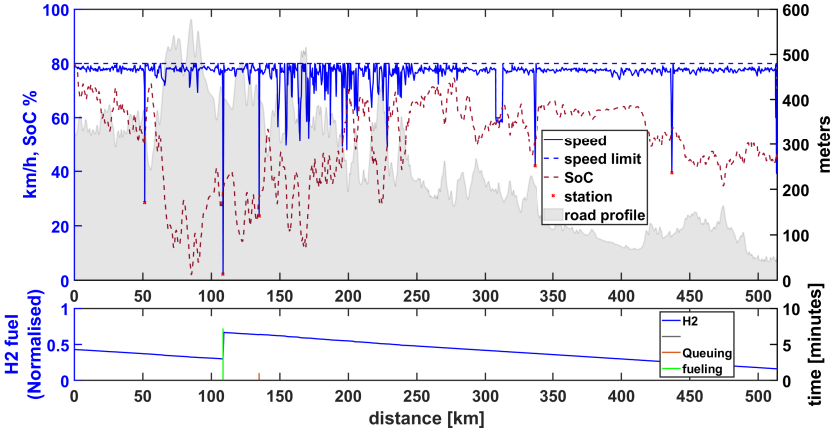

(c) Speed, SoC and fuel trajectories of the planned-PEM controller for a 40 ton truck

Figure 5.4: Speed, SoC and fuel comparison between the PEM controllers and the mission planner in case 2

Further, Figure 5.5 illustrates a comparison between the power split for the three controllers.

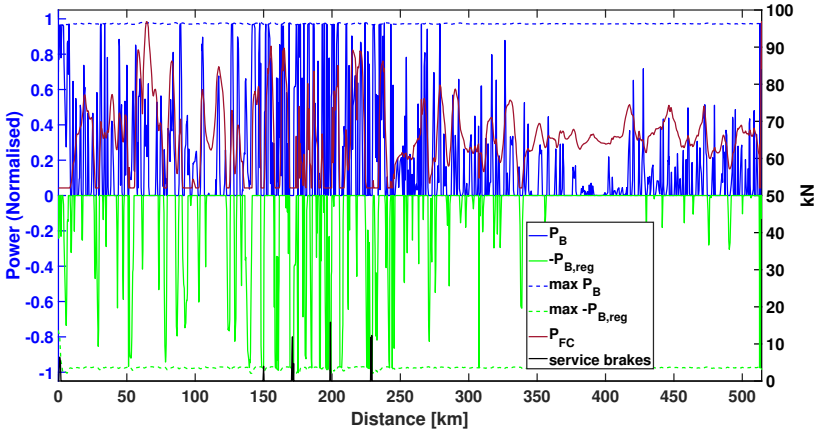

(a) Power split of the simple-PEM controller for a 40 ton truck

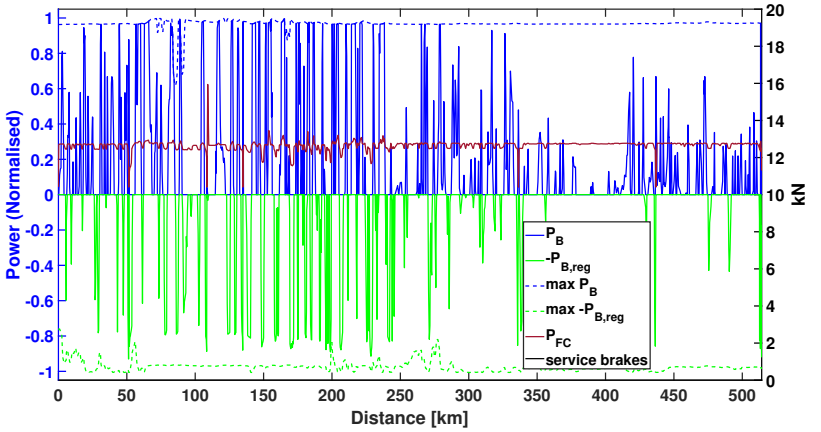

(b) Power split of the mission planner for a 40 ton truck

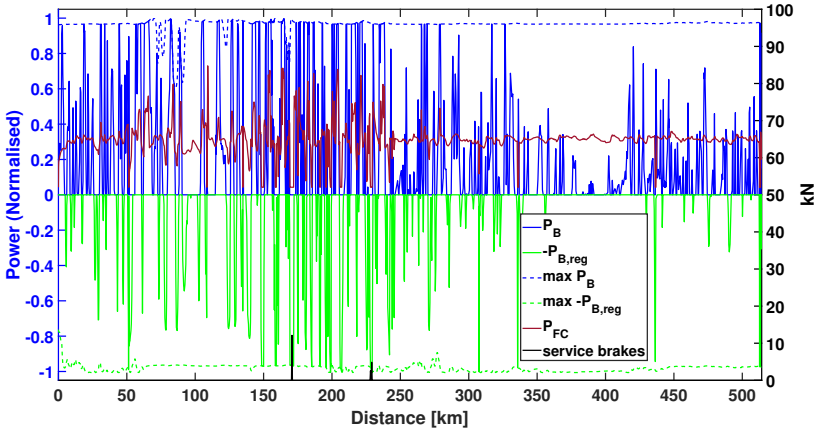

(c) Power split of the planned-PEM controller for a 40 ton truck

Figure 5.5: Power split comparison between the three controllers in case 2. P_B and $P_{B,reg}$ is the output- and regenerative braking power respectively. P_{FC} is the total power output from the fuel cell

Also, Figure 5.6 illustrates a comparison between fuel cell usage of the controllers with respect to fuel cell efficiency.

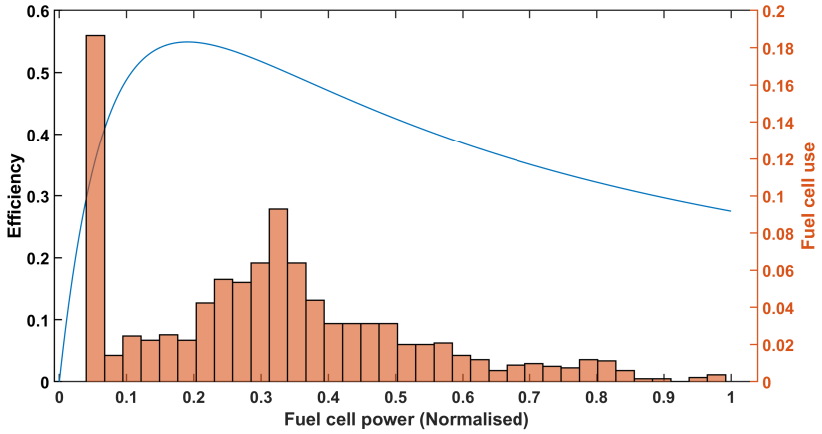

(a) Fuel cell usage of the simple-PEM controller for a 40 ton truck

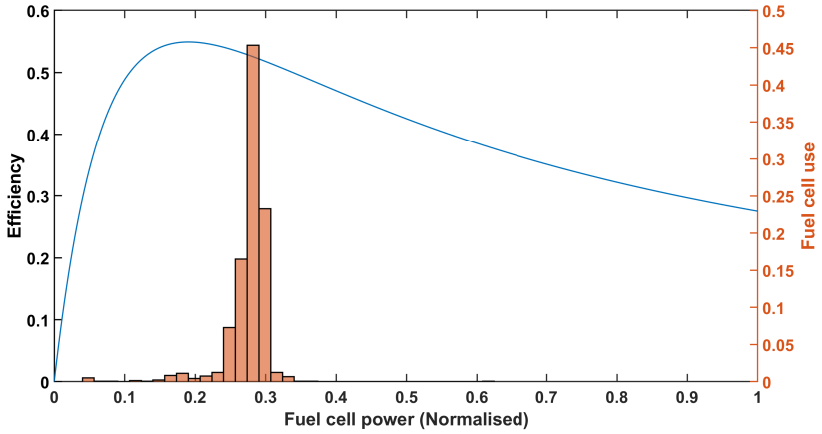

(b) Fuel cell usage of the mission planner for a 40 ton truck

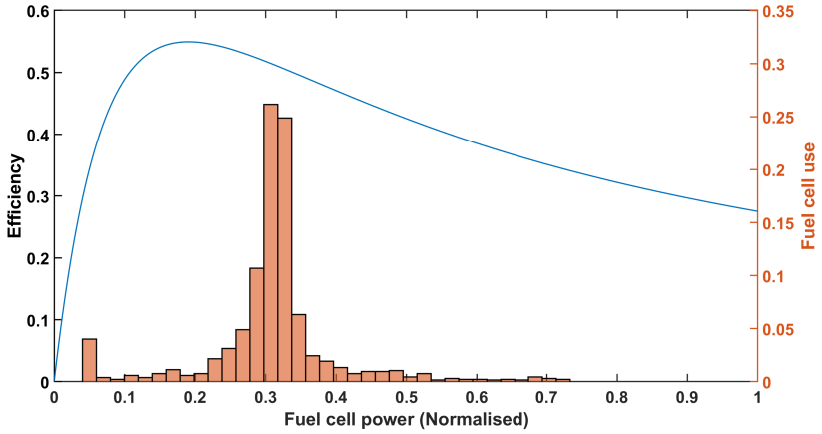

(c) Fuel cell usage of the planned-PEM controller for a 40 ton truck

Figure 5.6: Fuel cell usage comparison between the three controllers

A summary of the energy results can be seen in Table 5.4.

Table 5.4: Summary of energy results in case 2

Controller	Energy consumption (normalised)	Trip time [h]	Average speed [km/h]	Initial SoC [%]	Final SoC [%]
Simple-PEM	1	7.36	76.2	80	53
Mission planner	0.74	7.36	71.4	80	53
planned-PEM	0.83	6.9	76.2	80	46

Finally, Table 5.5 displays results in case 2 from a mission cost perspective. The trip cost metric has been normalised and set to 1 for the most expensive controller.

Table 5.5: Summary of mission results in case 2

Controller	Final available fuel (normalised)	Total trip cost (normalised)
Simple-PEM	0.23	1
Mission planner	0.23	0.72
planned-PEM	0.16	0.75

5.3 Case 3

This section outlines the result obtained when solving the problem formulation described in section 4.8, applied to Case 3 for the mission planner. Note that the driving cycle in this section is the same as in case 1. Figure 5.7 illustrates speed, SoC trajectories with refuelling decisions.

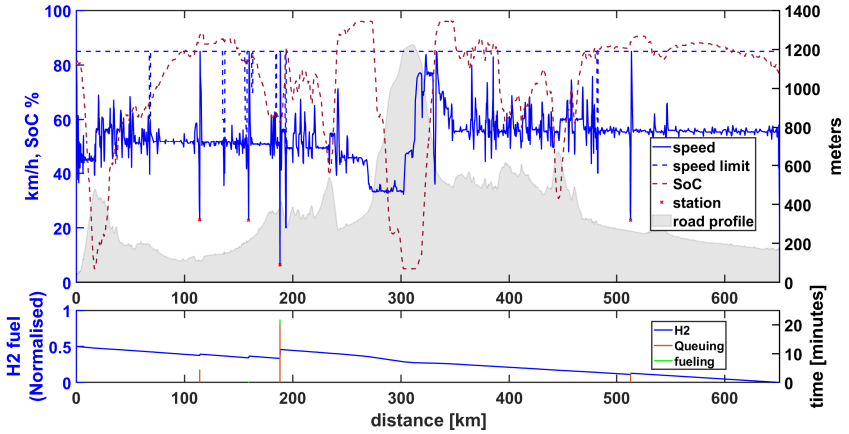

Figure 5.7: Speed, SoC and fuel trajectories of the mission planner for a 40 ton truck

Figure 5.8 illustrates the power split output from the controller.

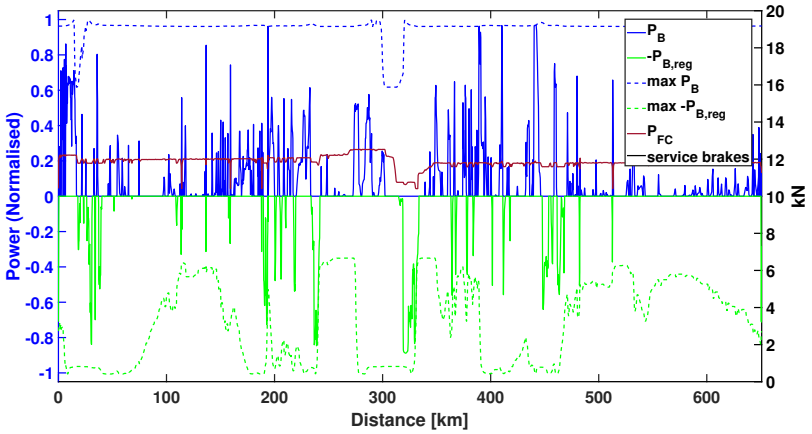

Figure 5.8: Power split of the mission planner for a 40 ton truck

Further, Figure 5.9 illustrates the fuel cell usage of the power split with respects to fuel cell efficiency

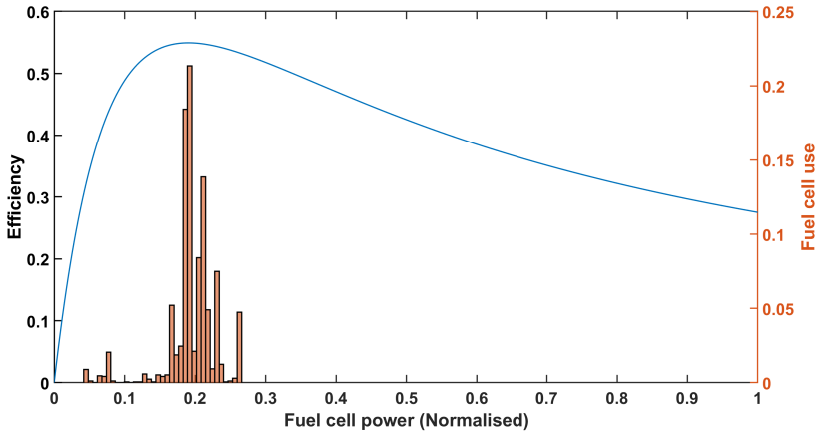

Figure 5.9: Fuel cell usage of the mission planner for a 40 ton truck

Table 5.6 presents the energy results for the mission planner in case 3. The results for the simple-PEM in case 1 are also included since it is the same driving cycle and allows easy comparisons.

Table 5.6: Energy results in case 1 for the simple-PEM and case 3 for the mission planner

Controller	Energy consumption (normalised)	Trip time [h]	Average speed [km/h]	Initial SoC [%]	Final SoC [%]
Simple-PEM	1	7.78	82.3	80	46
Mission planner	0.56	12.89	53.13	80	80

6
Discussion

6.1 Energy savings

The driving cycle in case 1 and case 3 is the more challenging of the two and more clearly demonstrates the benefit of having a preoptimised SoC reference. It can be seen when comparing Figure 5.1a with 5.1b and 5.1c, that the simple-PEM struggles to keep the reference speed due to low battery SoC which causes the fuel cell to stay at max power for the duration of the hill, as seen in Figure 5.2a. Another consequence of the simple-PEM strategy is sub optimal charging of battery SoC. Where the simple-PEM starts charging of the battery with the fuel cell before the truck reaches the large decline due to limited prediction horizon. Which then causes overcharging of the battery and subsequently having to use the friction brakes to avoid going over the speed limit. Comparing Figure 5.3a with 5.3c also demonstrates that it is possible to reduce energy consumption with a preoptimised SoC reference, due to the fuel cell operating with a higher efficiency. Also, Figure 5.2c shows a more stable fuel cell behaviour over the simple-PEM which leads to less degradation. All this is seemingly without any drawbacks since trip time is unaffected or even slightly improved as shown in Table 5.3.

The results from case 2 are less obvious in demonstrating benefits from a preoptimised SoC reference due to the transient behaviour of the terrain, but as seen in Table 5.4, the energy savings are clear. However, it does demonstrate benefits of a preoptimised fuelling plan. The simple-PEM controller implements (by design) the strategy of fuelling at the first available station. While the mission planner decides to refuel at the second station which is seen in Figures 5.4a and 5.4b respectively. Looking at Table 5.1, it is obvious that the second station is the more optimal choice. Assuming the available fuel is enough to reach it. It is also seen in Figure 5.4b that the time saved from fuelling without queuing is used by the mission planner to drive at a slower average speed. Which is an obvious conclusion that energy can be saved at the cost of trip time. However, that does not necessarily mean that total trip cost has been reduced by equally large proportion as seen in Table 5.5. This behaviour will vary depending on the cost that is related to time, which is a design parameter. The PEM-controller would have benefited from less aggressive tuning in this case when it comes to the 50% SoC reference. Doing so would have lowered the energy consumption of the controller. However, the planned-PEM controller uses the same tuning parameters so it can follow the optimal SoC trajectory. Therefore, allowing the PEM and planned-PEM controllers to have more freedom when it comes to SoC

trajectory would be against the purposes of this thesis.

By removing the time constraint from the mission planner, significant energy savings can be made as seen in Table 5.6 for case 3. This is of course, at the cost of trip time. Interestingly, the most optimal average speed is in range of $45 - 55$ km/h as seen in Figure 5.7. Looking at Figure 5.9 gives us a clue as to why this is. Since the fuel cell has a minimum power output that is above zero. The controller is forced to consume fuel but at a very low efficiency. Therefore, since it must consume fuel, it might as well be with the most efficiency which is around 20% of maximum power. This, coupled with the fact that time cost is also present in the optimisation, causes the planner to suggest to drive at some speed. It is not unreasonable to think that an increase in time cost would increase the average speed of the truck in this scenario, but the extent of this is not investigated.

6.2 Vehicle dynamics

Several transient vehicle dynamics, such as load transfer and wheel slip, are disregarded in the optimisation model. Including them in the model would drastically increases the problem size and complexity. The integration step size would also have to be reduced significantly to capture their effect. To the authors' belief, although no study is made, their impact on the optimal solution would be minimal. To support this claim, analogous models are used for similar cases in the literature, e.g. in [11] and [37].

6.3 ESS models

The fuel cell power model is approximated as a second order polynomial function. In reality, fuel cell performance degrades over time [38], and undergoes reversible degradation during operation [39]. The fuel cell efficiency and hydrogen consumption can readily be extended to consider specific fuel cell age. Performance degradation during operation due to reversible ageing is harder to include, but could likely be approximated.

The battery model is also readily modified to consider battery state of health. Regarding the SoC-dynamics, the authors' are aware of other models used in the literature, such as the one used in [11]. An analysis of model accuracy is not made in this thesis, but it should be considered that other models may be more, or less, accurate.

6.4 Refuelling

By introducing speed dependant refuelling dynamics, mixed integer optimisation is avoided but there are of course some drawbacks to this which need to be discussed. Firstly, the mission planner suggests to reduce speed at stations as low as possi-

ble without triggering the activation function $S_g(E)$ (4.35), if no fuelling is desired. Which is seen in Figures 5.4 and 5.7. This is of course sub optimal but can easily be remedied by rule based post processing of the mission planner. For instance, the planner suggests a large deviation from the speed limit and previous speed at station sample without actually triggering the activation function. This can then be considered an outlier and the suggestion can be removed. In case 2, this has not been done for the planned-PEM controller which follows the refuelling plan exactly as given by the mission planner.

Another aspect one has to take into account when optimising the refuelling plan is to include some final fuel constraint. In case 3, seen in Figure 5.7, there is no constraint on the final fuel amount and hence the amount of fuel left at the end is 0. This is of course optimal in a trip price sense but most likely not desirable in real world applications. A higher fuel consumption is also likely and using the mission planners suggestion in case 3 would then cause the truck to run out of fuel before the intended destination. Some hints of this are seen in Table 5.5, where the planned-PEM controller has finished the trip with 7 percentage points lower than the mission planner suggested.

6.5 NMPC structure

The approach in this thesis was to construct a controller which solves the entire problem jointly as all optimal states and control actions are dependent to each other. An option, which is commonly employed as it drastically reduces problem size, is to formulate a hierarchical NMPC problem. A possibility is to optimise speed and refuelling based on desired arrival time using F_T as control input and then optimise the power split in another NMPC program. A difficulty of this method is that the fuel consumption is dependant on the power split. The result of a hierarchical NMPC formulation is therefore that global optimality is lost, but the real-world practicality of the program is likely increased. The problem size of the mission planner is presently small enough to be used, especially with some optimisation, in a real-world application. Although, it may be necessary to split the problem if more details are added to the model.

6.6 Numerical optimisation

In this thesis, a nonlinear IP method is used to solve the optimisation problem, but there are many more alternatives. Sequential quadratic programming (SQP) is a promising alternative for a practical mission planer implementation as it is significantly faster for some problems [40]. The SQP method is, however, more suited for simple problems while IP methods are more robust for difficult problems. Therefore, the model may need to be augmented to use a SQP method.

The integrator used in this thesis is a first order explicit Runge-Kutta method,

which is applied at integration steps of hundreds of metres. Section 3.1 discusses the integration error and mentions that integration step size must be significantly lower than one to get moderate accuracy. The global integration error order $\mathcal{O}(h)$ is defined for integration step sizes smaller than one. For values larger than one, some constant related to the integration method and specific differential equation influences most. No evaluation of integration error or other methods is done in this thesis, but other methods are likely more suited to the application. Implicit Runge-Kutta methods have much larger stability regions, some are A-stable, and are therefore more suited for stiff problems and large integration steps. As the explicit Euler method does not diverge even for 1000 metre integration steps, the problem is likely not stiff. Despite this, use of implicit integrator may still be beneficial as the method may converge faster and with more accuracy. Another possibility, which makes the entire problem more suited for integration, is to sample in kilometres instead of metres. The integration steps are then less than one, or slightly larger than one, which should help obtain accurate integration results. One concern, if this is done, is the magnitude of the states and control inputs. Numerical optimisation solvers yield better results and converge faster for uniformly scaled problems in the range 0.01 to 100 [41].

6.7 Simulation

The mission planner is evaluated in the same model as the optimisation model. This has the implication that no verdict on the real-world efficacy of the mission planer can be made. It should however be noted that a high-fidelity simulation was made which showed results similar to the ones presented in this thesis. The simulation method used in this thesis is comparable to having a perfect model, and evaluating the benefit of global mission optimisation. A conclusion of the simulation is therefore that there are large potential benefits of preoptimising the entire driving mission.

7
Conclusion

This thesis proposes a NMPC-based supervisory controller for FCEVs, intended to be computed before the driving mission and possibly recomputed during it. The controller provides energy and cost-optimal vehicle speed, fuel cell power, battery power and battery SoC for a given driving mission. The powertrain outputs can be used by on-board energy management systems and thermal control systems for online decision making. The size and complexity of the problem is managed by reducing the mixed-integer NLP to a smooth and partially convexified NLP. The gear integer variable is removed from the optimisation problem by assuming efficiency-optimal gear at each feasible vehicle speed and traction effort pair. The integer refuelling decision is removed by introducing a smooth speed-dependent barrier function. Vehicle dynamics are approximated by smooth, convex and mostly quadratic functions. The mission planner is evaluated by simulating a 40-ton FCEV on two challenging driving cycles of 650 and 520 kilometres each. The 520 kilometres driving-cycle has refuelling stations placed along the route. Simulation shows that an energy-optimal receding horizon controller (3 kilometre prediction horizon) benefits greatly from tracking the SoC-reference and refuel plan provided by the mission planner. The energy savings are 13% for the 650 kilometre driving cycle and 17% for the 520 kilometre driving cycle. It is also found that the mission planner increases drivability in hilly areas and reduces friction break usage.

The study can be extended by including the thermal control system in the mission planner. This can be beneficial as the current planner may suggest driving behaviour and powertrain usage which the thermal control system inhibits during driving. Although, the practicality of an extended model must to evaluated as computation cost is increased. A study on several road and environment parameters, such as position-dependent rolling resistance, ambient temperature and wind speed, may be conducted as well. The fuelling dynamics are assumed linear, which they are not in reality, so an investigation of the model error is of interest. Finally, regenerative breaking is greatly simplified in this study, so it is advised to improve or tune that model.

Bibliography

[1] URL: https://unfccc.int/process-and-meetings/the-paris-agreement.

[2] URL: https://commission.europa.eu/strategy-and-policy/priorities-2019-2024/european-green-deal/delivering-european-green-deal_en.

[3] L. Guzzella and Antonio Sciarretta. *Vehicle propulsion systems. [electronic resource] : introduction to modeling and optimization.* Springer, 2007. ISBN: 3540746927. URL: https://search.ebscohost.com/login.aspx?direct=true&db=cat07472a&AN=clec.DAWVLE11349028&site=eds-live&scope=site&authtype=guest&custid=s3911979&groupid=main&profile=eds.

[4] Mengjun Gong et al. "Proton Exchange Membrane Fuel Cell as an Alternative to the Internal Combustion Engine for Emission Reduction: A Review on the Effect of Gas Flow Channel Structures". In: *Atmosphere* 14.3 (2023), p. 439.

[5] Xiaosong Hu et al. "Cost-optimal energy management of hybrid electric vehicles using fuel cell/battery health-aware predictive control". In: *ieee transactions on power electronics* 35.1 (2019), pp. 382–392.

[6] Lars Johannesson et al. "Predictive energy management of hybrid long-haul trucks." In: *Control Engineering Practice* 41 (2015), pp. 83–97. ISSN: 0967-0661. URL: https://search.ebscohost.com/login.aspx?direct=true&db=edselp&AN=S096706611500088X&site=eds-live&scope=site&authtype=guest&custid=s3911979&groupid=main&profile=eds.

[7] Ahad Hamednia et al. "Computationally efficient algorithm for eco-driving over long look-ahead horizons". In: *IEEE Transactions on Intelligent Transportation Systems* 23.7 (2021), pp. 6556–6570.

[8] Lars Johannesson et al. "Predictive energy management of hybrid long-haul trucks". In: *Control Engineering Practice* 41 (2015), pp. 83–97.

[9] Ahad Hamednia et al. "Optimal Thermal Management and Charging of Battery Electric Vehicles over Long Trips". In: *arXiv preprint arXiv:2210.03393* (2022).

[10] Seyed Amin Sajadi-Alamdari, Holger Voos, and Mohamed Darouach. "Nonlinear model predictive control for ecological driver assistance systems in electric vehicles". In: *Robotics and Autonomous Systems* 112 (2019), pp. 291–303.

[11] Saeid Zendegan et al. "Predictive battery state of charge reference generation using basic route information for optimal energy management of heavy-duty fuel cell vehicles". In: *IEEE Transactions on Vehicular Technology* 70.12 (2021), pp. 12517–12528.

[12] Yang Zhou, Alexandre Ravey, and Marie-Cécile Péra. "Real-time cost-minimization power-allocating strategy via model predictive control for fuel cell hybrid electric vehicles". In: *Energy Conversion and Management* 229 (2021), p. 113721.

[13] Shengwei Quan et al. “Real-time energy management for fuel cell electric vehicle using speed prediction-based model predictive control considering performance degradation”. In: *Applied Energy* 304 (2021), p. 117845.

[14] Ivan Pena-Arenas et al. “A mixed integer programming formulation for the truck drivers scheduling problem considering the European Union drivers rules.” In: *2021 IEEE 17th International Conference on Automation Science and Engineering (CASE), Automation Science and Engineering (CASE), 2021 IEEE 17th International Conference on* (2021), pp. 101–106. ISSN: 978-1-6654-1873-7. URL: https://search.ebscohost.com/login.aspx?direct=true&db=edseee&AN=edseee.9551634&site=eds-live&scope=site&authtype=guest&custid=s3911979&groupid=main&profile=eds.

[15] Asvin Goel. “Truck Driver Scheduling in the European Union.” In: *Transportation Science* 44.4 (2010), pp. 429–441. ISSN: 00411655. URL: https://search.ebscohost.com/login.aspx?direct=true&db=bsu&AN=55413561&site=eds-live&scope=site&authtype=guest&custid=s3911979&groupid=main&profile=eds.

[16] R. Rajamani. *Vehicle Dynamics and Control*. Mechanical Engineering Series. Springer US, 2011. ISBN: 9781461414339. URL: https://books.google.se/books?id=cZJFDox4KuUC.

[17] Germana Paterlini and Sermet Yucel. “Rolling resistance validation”. In: *Minnesota Department of Transportation, Tech. Rep* (2015).

[18] May 2006. URL: https://physics.nist.gov/MajResFac/NIF/pemFuelCells.html.

[19] Jean-Paul Kone et al. “Three-dimensional multiphase flow computational fluid dynamics models for proton exchange membrane fuel cell: A theoretical development”. In: *The Journal of Computational Multiphase Flows* 9.1 (2017), pp. 3–25.

[20] Sahra Hamdollahi and Luo Jun. “A Review on Modeling of Proton Exchange Membrane Fuel Cell”. In: *Chemical Industry & Chemical Engineering Quarterly* 29.1 (2023), pp. 61–74.

[21] Lindiwe Khotseng. “Fuel Cell Thermodynamics”. In: *Thermodynamics and Energy Engineering*. Ed. by Petrică Vizureanu. Rijeka: IntechOpen, 2019. Chap. 1. DOI: 10.5772/intechopen.90141. URL: https://doi.org/10.5772/intechopen.90141.

[22] Huy Quoc Nguyen and Bahman Shabani. “Proton exchange membrane fuel cells heat recovery opportunities for combined heating/cooling and power applications”. In: *Energy Conversion and Management* 204 (2020), p. 112328. ISSN: 0196-8904. DOI: https://doi.org/10.1016/j.enconman.2019.112328. URL: https://www.sciencedirect.com/science/article/pii/S0196890419313354.

[23] VB Avakov et al. “Lifetime prediction for the hydrogen–air fuel cells”. In: *Russian Journal of Electrochemistry* 51 (2015), pp. 570–586.

[24] Ivan Cowie and Ivan Cowie. *All about batteries, part 12: Lithium titanate (LTO)*. Jan. 2015. URL: https://www.eetimes.com/all-about-batteries-part-12-lithium-titanate-lto/.

[25] Xuebing Han et al. “Cycle Life of Commercial Lithium-Ion Batteries with Lithium Titanium Oxide Anodes in Electric Vehicles”. In: *Energies* 7.8 (July 2014), pp. 4895–4909. ISSN: 1996-1073. DOI: 10.3390/en7084895. URL: http://dx.doi.org/10.3390/en7084895.

[26] Feng Leng, Cher Tan, and Michael Pecht. “Effect of Temperature on the Aging rate of Li Ion Battery Operating above Room Temperature”. In: *Scientific reports* 5 (Aug. 2015), p. 12967. DOI: 10.1038/srep12967.

[27] Thomas Waldmann et al. “Temperature dependent ageing mechanisms in Lithium-ion batteries – A Post-Mortem study”. In: *Journal of Power Sources* 262 (2014), pp. 129–135. ISSN: 0378-7753. DOI: https://doi.org/10.1016/j.jpowsour.2014.03.112. URL: https://www.sciencedirect.com/science/article/pii/S0378775314004352.

[28] JG Qu, ZY Jiang, and JF Zhang. “Investigation on lithium-ion battery degradation induced by combined effect of current rate and operating temperature during fast charging”. In: *Journal of Energy Storage* 52 (2022), p. 104811.

[29] Laxman Timilsina et al. “Battery Degradation in Electric and Hybrid Electric Vehicles: A Survey Study”. In: *IEEE Access* (2023).

[30] J.B. Rawlings, D.Q. Mayne, and M. Diehl. *Model Predictive Control: Theory, Computation, and Design*. Nob Hill Publishing, 2017. ISBN: 9780975937730. URL: https://books.google.se/books?id=MrJctAEACAAJ.

[31] Moritz Diehl, Hans Joachim Ferreau, and Niels Haverbeke. “Efficient numerical methods for nonlinear MPC and moving horizon estimation”. In: *Nonlinear model predictive control: towards new challenging applications* (2009), pp. 391–417.

[32] Tor A Johansen. “Introduction to nonlinear model predictive control and moving horizon estimation”. In: *Selected topics on constrained and nonlinear control* 1 (2011), pp. 1–53.

[33] Alexander Domahidi and Juan Jerez. *FORCES Professional*. Embotech AG, url=https://embotech.com/FORCES-Pro. 2014–2019.

[34] A. Zanelli et al. “FORCES NLP: an efficient implementation of interior-point... methods for multistage nonlinear nonconvex programs”. In: *International Journal of Control* (2017), pp. 1–17.

[35] H2-Mobility. *70 MPa Hydrogen Refuelling Station Standardization: Functional Description of Station Modules*. 2010.

[36] Fabian Grüger et al. “Carsharing with fuel cell vehicles: Sizing hydrogen refueling stations based on refueling behavior.” In: *Applied Energy* 228 (2018), pp. 1540–1549. ISSN: 0306-2619. URL: https://search.ebscohost.com/login.aspx?direct=true&db=edselp&AN=S0306261918310419&site=eds-live&scope=site&authtype=guest&custid=s3911979&groupid=main&profile=eds.

[37] Longlong Zhu et al. “Optimization based adaptive cruise control and energy management strategy for connected and automated fchev”. In: *IEEE Transactions on Intelligent Transportation Systems* 23.11 (2022), pp. 21620–21629.

[38] Bartosz Ceran et al. “Aging effects on modelling and operation of a photovoltaic system with hydrogen storage”. In: *Applied Energy* 297 (2021), p. 117161.

[39] Johannes Tjønnås et al. “Control of reversible degradation mechanisms in fuel cells: Mitigation of CO contamination”. In: *IFAC-PapersOnLine* 49.7 (2016), pp. 302–307.

[40] URL: `https://forces.embotech.com/Documentation/high_level_interface/index.html#sequential-quadratic-programming-algorithm`.

[41] URL: `https://web.casadi.org/blog/nlp-scaling/`.

A

Appendix 1

A.1 Mission problem formulation

Below follows the complete formulation of the mission planner optimisation with the objective of minimising the cost of a mission. Relations that follow from Section 4 are not repeated to condense the formulation.
Minimize,

$$\sum_{k=1,k\neq s_i}^{N} c_\delta\delta(k) + c_{H2}\left(H_{con}(k) - H_{con}(k-1)\right) + c_t\left(t(k) - t(k-1)\right) + c_b F_{break}(k) + \\ + \sum_{k=s_0}^{s_N} c_\delta\delta(k) + c_{stat}\left(H_{con}(k-1) - H_{con}(k)\right) S_g\left(\sqrt{2E(k)}\right) + c_t\left(t(k) - t(k-1)\right) + c_f S_g\left(\sqrt{2E(k)}\right) \tag{A.1}$$

Subject to equality constraints,

$$t(k+1) = t(k) + \frac{1}{\sqrt{2E(k)}} + S_g\left(\sqrt{2E(k)}\right)\cdot q_t(k) \tag{A.2a}$$

$$E(k+1) = F_T(k) - F_{break}(k) - \frac{A_{v,f}C_d\rho_{air}}{m}E(k) - C_{rr}g\cos(\alpha(k)) - g\sin(\alpha(k)) \tag{A.2b}$$

$$SoC(k+1) = SoC(k) + \frac{F_{B,reg}(k) + \eta_{DC}F_{FC\to B}(k) - F_B(k)}{C_b U_{OC}(SoC(k))} - P_{B,loss}(k) \tag{A.2c}$$

$$H_{con}(k+1) = H_{con}(k) + \frac{a_0}{\sqrt{2E(k)}} + a_1 F_{FC}(k) + a_2\sqrt{2E(k)}\,F_{FC}(k)^2 - s\frac{s_f}{\sqrt{2E(k)}}S_g(\sqrt{2E(k)}) \tag{A.2d}$$

inequality constraints,

$$P_{FC}^{min} \leq \left(F_{FC} + F_{FC\to B}\right)\sqrt{2E(k)} \leq P_{FC}^{max} \tag{A.3a}$$

$$P_B^{min}(SoC(k)) \leq F_B\sqrt{2E(k)} \leq P_B^{max}(SoC(k)) \tag{A.3b}$$

$$\sqrt{2E(k)} \leq v_{max}(k) \tag{A.3c}$$

$$F_B(k)F_{B,reg}(k) \leq 0 \tag{A.3d}$$

$$F_{T,min}(\sqrt{2E(k)}) \leq F_T(k) \leq F_{T,max}(\sqrt{2E(k)}) \tag{A.3e}$$

$$t(k) \leq t_{max} \tag{A.3f}$$

A.2 PEM problem formulation

Below follows the complete formulation of the PEM optimisation with the objective of minimising speed and SoC references and also hydrogen consumption. Both PEM controllers follow the same problem formulation.
Minimize,

$$\sum_{k=1}^{N} c_\delta \delta(k) + c_{H2}\left(H_{con}(k) - H_{con}(k-1)\right) + c_{SoC}\left(ref_{SoC}(k) - SoC(k)\right)^2 + \\ + c_v\left(\sqrt{2E(k)} - v_{lim}\right)^2 + c_b F_{break}(k) \quad \text{(A.4)}$$

where c_{SoC} and c_v are costs for deviating from the SoC and speed references respectively,
Subject to equality constraints,

$$t(k+1) = t(k) + \frac{1}{\sqrt{2E(k)}} + S_g\left(\sqrt{2E(k)}\right) \cdot q_t(k) \quad \text{(A.5a)}$$

$$E(k+1) = F_T(k) - F_{break}(k) - \frac{A_{v,f} C_d \rho_{air}}{m} E(k) - C_{rr} g \cos(\alpha(k)) - g \sin(\alpha(k)) \quad \text{(A.5b)}$$

$$SoC(k+1) = SoC(k) + \frac{F_{B,reg}(k) + \eta_{DC} F_{FC\to B}(k) - F_B(k)}{C_b U_{OC}(SoC(k))} - P_{B,loss}(k) \quad \text{(A.5c)}$$

$$H_{con}(k+1) = H_{con}(k) + \frac{a_0}{\sqrt{2E(k)}} + a_1 F_{FC}(k) + a_2\sqrt{2E(k)}\, F_{FC}(k)^2 - s\frac{s_f}{\sqrt{2E(k)}} S_g(\sqrt{2E(k)}) \quad \text{(A.5d)}$$

inequality constraints,

$$P_{FC}^{min} \le \left(F_{FC} + F_{FC\to B}\right)\sqrt{2E(k)} \le P_{FC}^{max} \quad \text{(A.6a)}$$

$$P_B^{min}(SoC(k)) \le F_B\sqrt{2E(k)} \le P_B^{max}(SoC(k)) \quad \text{(A.6b)}$$

$$\sqrt{2E(k)} \le v_{max}(k) \quad \text{(A.6c)}$$

$$F_B(k) F_{B,reg}(k) \le 0 \quad \text{(A.6d)}$$

$$F_{T,min}(\sqrt{2E(k)}) \le F_T(k) \le F_{T,max}(\sqrt{2E(k)}) \quad \text{(A.6e)}$$

$$t(k) \le t_{max} \quad \text{(A.6f)}$$

DEPARTMENT OF ELECTRICAL ENGINEERING
CHALMERS UNIVERSITY OF TECHNOLOGY
Gothenburg, Sweden
www.chalmers.se

CHALMERS
UNIVERSITY OF TECHNOLOGY